

Geometric and Electronic Structures of
Graphene Hybrid Structure under
an External Electric Field

Manaho Matsubara

February 2019

Geometric and Electronic Structures of Graphene Hybrid Structure under an External Electric Field

Manaho Matsubara

Doctoral Program in
Nano-Science and Nano-Technology

Submitted to the Graduate School of
Pure and Applied Sciences
in Partial Fulfillment of the Requirements
for the Degree of Doctor of Philosophy in Science

at the
University of Tsukuba

Abstract

A honeycomb network of graphene consisting of sp^2 C atoms endows it with remarkable physical properties, such as high mechanical strength, high thermal conductivity, and high carrier mobility. On the other hand, because of its planar sheet structure, these properties are sensitive to external perturbations, such as adsorption of foreign materials, atomic defects, and external fields. In particular, the electronic properties near the Fermi level are fragile. The fact implies that such perturbations further extend the science and technology associated with graphene. Indeed, graphene has no longer possess linear dispersion bands at the Fermi level in some cases, when it forms hybrid structures with insulating substrates, atoms, or molecules. Moreover, the external fields also modulate the electronic structures: the magnetic field causes the Landau level by quantizing the energy band, and the electric field opens the band gap in bilayer graphene. Although much effort has been devoted to elucidate the effect of such perturbations on the electronic properties of graphene and its hybrids, the knowledge is restricted to systems containing single disturbance. On the other hand, in practical situations of experiments and applications, graphene basically forms the hybrid structures with two or more external disturbances. Here, we casted a spotlight on graphene adsorbing foreign materials such as metal nanoparticles and molecules under the electric field. We also studied the electronic properties of N-doped graphene with various conformations under the external electric field. To get the electronic properties of graphene hybrids under the field, we used the density functional theory combined with the effective screening medium method. These studies may add the fundamental knowledge about the electronic properties of graphene forming hybrid structures with foreign materials under the electric field, which certainly advances science and technology of graphene and graphene based hybrids.

Our calculations show that carrier accumulation in graphene adsorbing Al nanoparticles strongly depends on the carrier species and the relative arrangement of charged impurities with respect to the electrode. In the case of Al nanoparticles sandwiched between graphene and the electrode, the nanoparticles prevent the carrier injection in graphene, whereas the carriers are injected into graphene when the nanoparticles are located opposite side of graphene to the electrode. We also found that the equilibrium spacing between Al nanoparticles and graphene depends on their arrangement to the electrode and carrier species. Al nanoparticles are not bound to graphene under the high carrier concentrations, when Al particles are sandwiched between graphene and electrode. In contrast, the spacing monotonically decreases with increasing the hole concentration when the nanoparticles are situated on the opposite side of graphene to the electrode. We further studied the energetics and geometries of CO and CO₂ molecules adsorbed on graphene with regard to carrier density and species injected under the external electric field for providing guiding principle to tune and control the binding properties of these molecules to graphene using the electric field. Our calculations show that the energetics

and stable binding structures of CO and CO₂ adsorbed on graphene are sensitive to the carrier density and species injected by the counter gate electrode. The carriers can control the binding energy and stable conformations of these molecules on graphene by tuning the carrier density and species.

Because N-doped graphene is one of representative graphene-based hybrids exhibiting interesting variation in their electronic structures, we focus on the field effect on the electronic properties of N-doped graphene by conducting first-principle total-energy calculations. Our calculations show that the electronic states near the Fermi level are sensitive to carrier injection by the external electric field. The electronic state associated with the saturated dangling bond of N shift upward and downward upon electron and hole injections, respectively, following the Fermi level shift caused by the carrier injection in N-doped graphene. In contrast, the electronic states associated with nonbonding π states almost retain their energy upon carrier injection by the external electric field. The results indicate that the band-filling of the nonbonding π states of N-doped graphene is controllable by adjusting the external electric field.

Acknowledgements

I would like to express my great appreciation to Professor Susumu Okada for his continuing guidance, discussions, and encouragements throughout the present work.

I would also like to offer my special thanks to Professor Takazumi Kawai for fruitful discussions.

My special thanks are extended to the all member of the laboratory under Professor Okada, particularly Dr. Mina Maruyama, Ms. Yanlin Gao, Ms. Airi Yasuma, Mr. Hisaki Sawahata, Mr. Kazufumi Yoneyama, and Mr. Yasumaru Fujii for many discussions and advices.

I would like to thank laboratory secretary, Ms. Reiko Wada, for her supports.

My special thanks goes to my superiors and my colleagues in TOSHIBA corporation, especially Mr. Motoharu Shiiki and Mr. Yuta Abe for their great and laborious support.

To my father and mother, I am deeply grateful for everything they have done for me.

Contents

Abstract	i
1 Introduction	1
2 Calculation Methods	6
2.1 Density Functional Theory	6
2.1.1 Density Variational Principle	6
2.1.2 Kohn-Sham Equation	7
2.2 Exchange-correlation Energy Functional	9
2.2.1 Local Density Approximation	10
2.2.2 Generalized Gradient Approximation	10
2.3 Plane-wave Basis Set	11
2.4 Pseudopotential	12
2.4.1 Norm-conserving Pseudopotential	13
2.4.2 Ultrasoft Pseudopotential	14
2.5 Effective Screening Medium Method	16
3 Graphene Adsorbing Al_x Nanoparticles	19
3.1 Introduction	19
3.2 Computational Parameters and Structural Models	20
3.3 Carrier Distribution and Electronic Properties	21
3.4 Energetics and Geometric Structures	25
3.5 Summary	28
4 Graphene Adsorbing CO₂ and CO Molecules	30
4.1 Introduction	30
4.2 Computational Parameters and Structural Models	31
4.3 Energetics and Geometric Structures Under an External Electric Field	34
4.4 Carrier Distribution	36
4.5 Electronic Structures	39
4.6 Summary	40
5 N-doped Graphene	41
5.1 Introduction	41
5.2 Computational Parameters and Structural Models	42
5.3 Electronic Structure	43
5.4 Summary	47

6	Conclusions	50
A	Hohenberg-Kohn Theorems	52
	Bibliography	54

Chapter 1

Introduction

Graphite is a representative carbon allotrope possessing a layered structure in which C sheets of hexagonal covalent networks are stacked each other via weak interlayer interaction [Fig. 1.1]. According to the weak interlayer interaction, graphite has a lot of polymorphs with regard to their interlayer stacking arrangements, such as the ABA stacking (Bernal stacking), ABC stacking (Rhombohedral stacking), and turbostratic stacking [1, 2]. Low energy electronic structures of these graphite polymorphs depend on these stacking difference, despite the weak interlayer interaction [3]. The weak interlayer interaction allows us to peel off the single layer of hexagonal C network from bulk graphite [4]. An exfoliated single layer is now known to be graphene as an ultimate version of two-dimensional materials because of its one atom thickness. The unit cell of graphene, with a lattice constant of 0.246 nm or bond length of 0.142 nm, contains two independent C atomic sites each of which forms triangular lattice and is connected via strong covalent bonds with its three adjacent sites by σ states of C atom with sp^2 hybridization. The honeycomb covalent network arising from tightly bound σ electrons endows graphene with remarkable mechanical properties [5–8]: graphene has high breaking strength of 42 N/m and thermal conductivity over 1000 W/mK at room temperature. In addition to the mechanical properties arising from σ electrons, π (p_z) electrons, which are distributed normal to the sheet and itinerate throughout the hexagonal network, lead to peculiar electronic structure near the Fermi level [9–11]: graphene has a pair of linear dispersion bands at six corners of the hexagonal Brillouin zone, leading to the semiconducting electronic structure with vanishing electron density at the Fermi level. The electron near the corners in graphene behaves as a massless Dirac fermion. Therefore, carriers on graphene are expected to exhibit high mobility over 200,000 cm²/Vs at low temperature [12, 13] and unusual quantum Hall effects [14, 15]. Therefore, graphene is now keeping a premier position in the field of nanoscale sciences and technologies.

Owing to the unusual geometric and electronic properties, graphene is also regarded as a starting material for designing various derivatives by forming hybrid structures with foreign materials and external environments. Boundary conditions, such as open and periodic boundary conditions resulting in graphene nanoribbons and carbon nanotubes, respectively, make these graphene derivatives semiconductors, metals, or ferromagnets depending on the resultant network topologies [16–20]. Furthermore, the electronic

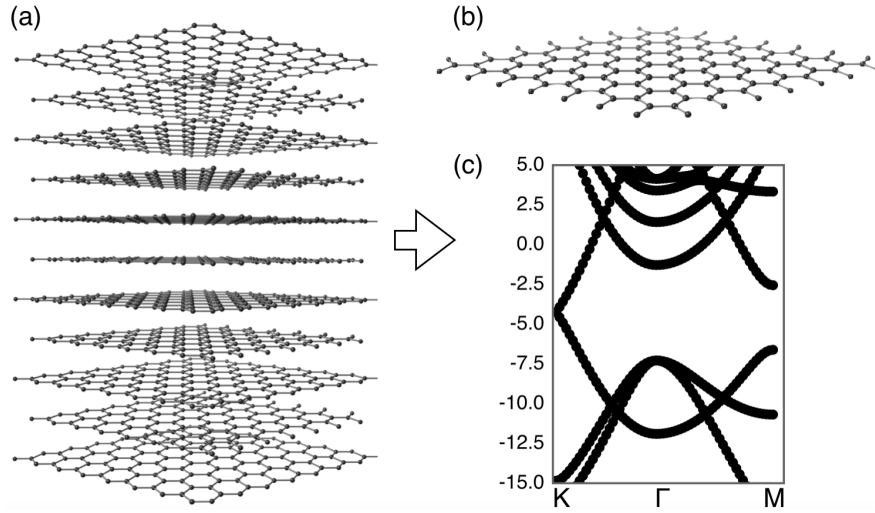


FIGURE 1.1: (a) A structure of graphite. Each of layers consists of hexagonal C networks. (b) A single layer peels off from graphite with hexagonal C network, which is so-called Graphene. (c) Band structure of graphene. The energy is measured from the vacuum energy.

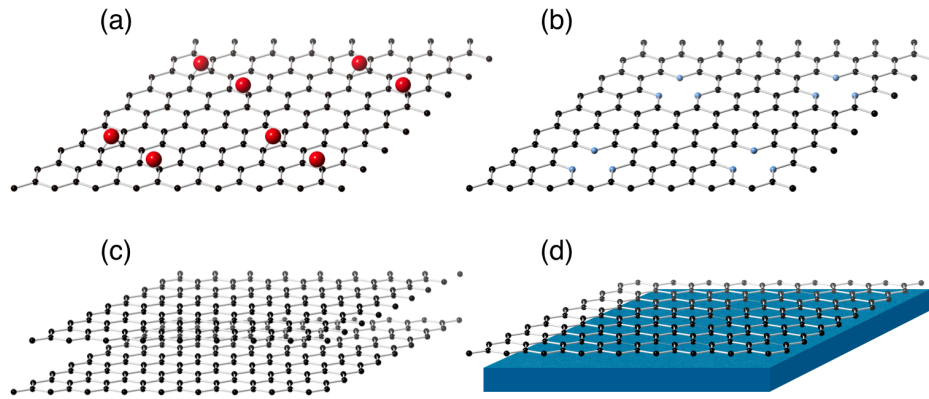


FIGURE 1.2: Hybrid structures of graphene: (a) graphene adsorbing impurities, (b) atom-doped graphene, (c) bilayer graphene, and (d) graphene adsorbed on insulating substrate.

properties of graphene are sensitive to the external environment [Fig. 1.2]. Atoms and molecules could be adsorbed on graphene surfaces because all atomic sites of graphene are exposed to the environment. Molecular and atomic adsorbates substantially affect physical and chemical properties of graphene [21, 22]. Chemisorption of atoms and molecules causes nonbonding π states at the Fermi level because of the sub-lattice imbalance in the bipartite network of graphene. Indeed, fluorination and oxidization have been achieved, and these complexes exhibit different nature in their electronic structure [Fig. 1.3] [23–27]. Furthermore, depending on the mutual arrangements of the adjacent adsorbates, graphene is not zero-gap semiconductor but the finite gap semiconductor of which band gap is inversely proportional to the density of the adsorbates [28] and depends on their arrangement [29]. In addition to the modulation of the intrinsic electronic structure of graphene, adsorbates also cause further modulation of the electronic properties of graphene in some cases. Owing to the electrostatic potential modulation by the adsorbed molecules, the Fermi level of graphene adsorbing molecules is slightly

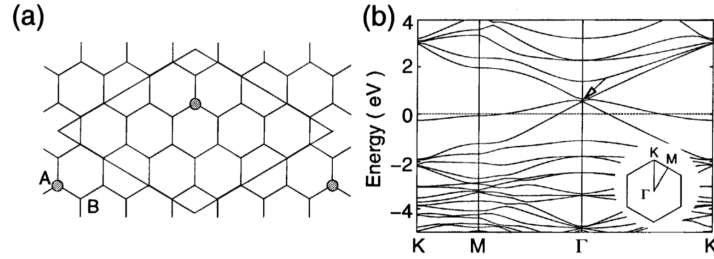


FIGURE 1.3: (a) The geometric structure of $C_{24}F$. Shaded circles denote fluorine atoms adsorbed on carbon atoms. (b) Band structure of the $C_{24}F$ compound. The energy is measured from the Fermi energy [23].

shifted depending on the molecular species and conformations, and the low energy spectra of graphene is found to strongly depend on the molecular conformation, even though they are adsorbed on graphene via weak interaction [Fig. 1.4] [30–32]. Furthermore, molecules or atoms can donate electron into or accept electron from graphene, leading to the substantial shift of the Fermi level. Indeed, it is confirmed that the Hall resistance as a function of the gate voltage depends on the adsorbate concentrations [33]. Although C atoms in graphene are tightly bound each other via strong σ covalent bonds, vacancies, which are regarded as the negative atoms or clusters, are implanted into graphene network, forming interesting complexes possessing unusual electronic structures. As the case of graphene chemically adsorbing atoms, the defective graphene or porous graphene have unusual electronic structures which are absent in the pristine graphene, depending on the network topology of the graphitic region and on the arrangement of the pores or defects [34]. The porous graphene occasionally possesses peculiar electronic energy bands at or near the Fermi level, which consist of the Dirac cone and flat band through the Brillouin zone, allowing these complex constituent materials of the magnetic and spintronic devices [35, 36]. In addition to the pristine defective and porous graphene, the edge C atomic sites around the defects are substituted by N atoms, leading to the N-doped graphene which possesses the catalytic activity [37, 38]. The electronic structures of N-doped graphene are sensitive to the defect structure, such as graphitic, pyridinic, and pyrrolic structures [39]. The fact implies that the energetics to form hybrids with atoms or molecules also depends on the defect species and conformations. For instance, the pyridinic defect provides the largest adsorption energy for H atoms among possible N-doped graphene [40].

An electronic field is another important factor to modulate the electronic structure of graphene. Bilayer graphene is known to be a semiconductor with finite band gap in the presence of an external electric field normal to the plane [41–46]. In this case, the electrostatic potential difference between two layers shifts the linear bands upward/downward and these bands repel each other owing to the symmetry requirement. The gap obtained by the density functional theory (DFT) calculation gradually increases up to 0.27 eV at the field of 0.6 V/Å [Fig. 1.5]. In addition to the metal-semiconductor transition induced by low and moderate electric fields, the bilayer graphene again has metallic character, in which the carriers totally differ from those of the pristine graphene, under the electric field stronger than 1.00 V/Å. Thus, in the case of bilayer graphene, there are successive transitions (i.e., a metal-semiconductor-metal transition) under the electric field [47].

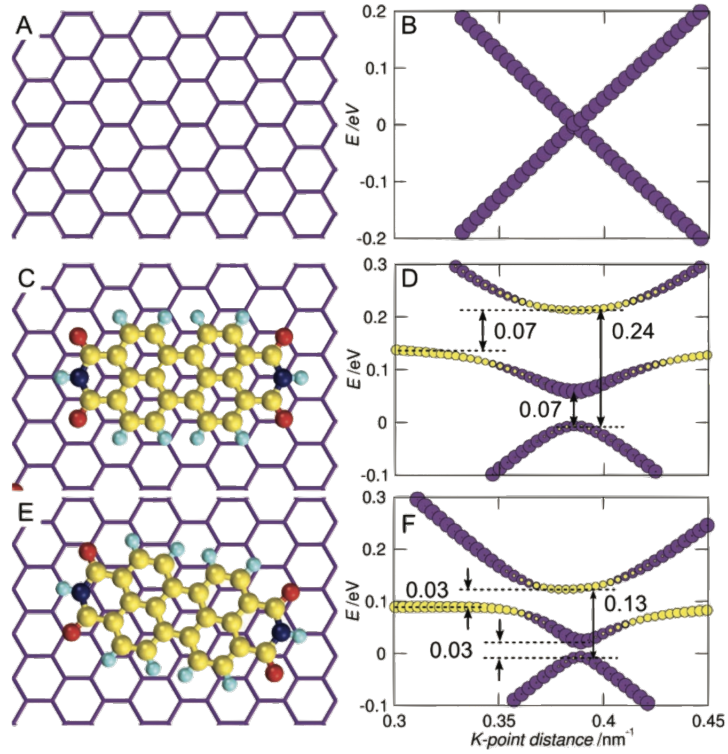


FIGURE 1.4: Band structures of (B) pristine graphene, (D) graphene adsorbing molecule, and (F) graphene adsorbing rotated molecule, corresponding to the geometries (A), (C), and (E), respectively [32].

As stated above, the each external disturbance, such as defects, atoms, molecules, substrates, and external electric field, affects the zero-gap semiconducting electronic property of graphene. On the other hand, little is known about the electronic properties of graphene under simultaneously two or more external disturbances, although graphene intrinsically feels two or more external disturbances in practical situations. For instance, graphene in electronic devices intrinsically contains impurities (adsorbates and defects) or supporting substrates, together with the external electric field. In such cases, it is uncertain whether the electronic structure modulation is the simple superposing of those induced by each disturbance or not. Indeed, a bilayer graphene consisting of pristine and defective layers has finite band gap with flat bands associated with the defects, so that the electronic structure modulation depends on the mutual arrangement of the bilayer graphene in terms of the electric field [48].

Therefore, in this thesis, we aim to elucidate the effects of the impurities on the electronic properties of graphene under the external electric field and investigate the change in the stable structure of graphene adsorbing impurities under the electric field, which provides the guiding principle to control the physical properties of graphene in its hybrid structures. In addition, we also reveal the electronic structure of N-doped graphene and clarify the possibility of Fermi level tuning of N-doped graphene under the carrier injection induced by the gate electrode using the DFT with the effective screening medium method.

The thesis is organized as following. In Chapter 2, we review calculation methods used in this thesis. Chapter 3 shows the electronic and geometric structures of graphene

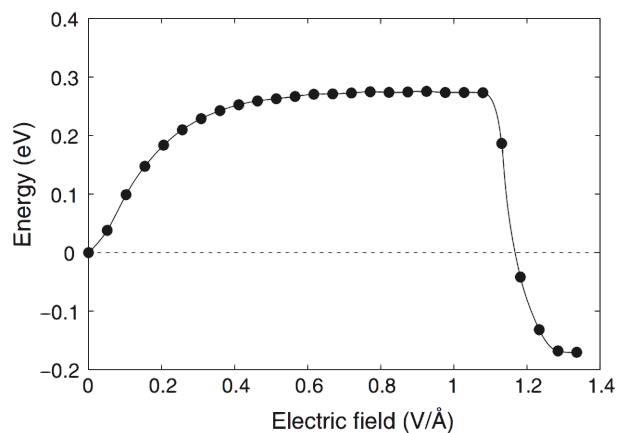


FIGURE 1.5: Energy gap of bilayer graphene as a function of the external electric field [47]. Energy measures from the Fermi level energy.

adsorbing metallic nanoparticles under the external electric field with the field-effect transistor structure. Chapter 4 demonstrates the electronic and geometric structures of CO and CO₂ molecules adsorbed on graphene under the external electric field. Chapter 5 shows the electronic properties of N-doped graphene with graphitic, pyrrolic, and pyridinic structures in terms of the field-effect carrier injection. Finally, we conclude the thesis in Chapter 6.

Chapter 2

Calculation Methods

In this Chapter, we present the calculation methods used in this thesis. All calculations are conducted using the density functional theory (DFT), which is one of the representative approaches to get geometric and electronic structures of matters without the aid of any empirical parameters. For practical application of DFT, we use the local density approximation and generalized gradient approximation for describing exchange-correlation potential. We adopted ultrasoft pseudopotentials for describing the electron-ion interaction to reduce the calculation cost. We use the effective screening medium method to calculate the materials under the particular electrostatic boundary conditions using the DFT with plane-wave basis set.

2.1 Density Functional Theory

The DFT is an effective approach to calculate the electronic structures of many-body electron systems. The DFT has been developed by Hohenberg, Kohn, and Sham [49–53]. Hohenberg and Kohn have provided that the total energy is a unique functional of electron density. Kohn and Sham have shown how to replace the many-electron problem by an equivalent one-electron problem, in which each electron is moving in an effective potential. In the following subsection, we describe the DFT formalism.

2.1.1 Density Variational Principle

A Hamiltonian \hat{H} of the N-electron system in Hartree atomic unit is written as

$$\begin{aligned}\hat{H} &= \hat{T} + \hat{V}_{ee} + \hat{V}_{\text{ext}} \\ &= -\frac{1}{2} \sum_{i=1}^N \nabla_i^2 + \frac{1}{2} \sum_{j \neq i=1}^N \frac{1}{|\mathbf{r}_i - \mathbf{r}_j|} + \sum_{i=1}^N V_{\text{ext}}(\mathbf{r}_i)\end{aligned}\quad (2.1)$$

where \hat{T} , \hat{V}_{ee} , and \hat{V}_{ext} are the kinetic energy, the electron-electron interaction, and the external potential, respectively.

Hohenberg and Kohn provided the way to calculate the total energy of the N-electron system using the electron density, instead of treating N-body wave functions. In the Hohenberg-Kohn theorem, it is stated that the ground state electron density is uniquely determined by the external potential. Additionally, the global minimum value of a total energy functional in terms of the electron density corresponds to the exact ground state energy of the system, and the electron density minimizing the functional is the exact ground state density. The proof of the Hohenberg-Kohn theorems is described in Appendix A. The total energy can be written as

$$\begin{aligned}
 E[\rho] &= \langle \Psi | \hat{T} + \hat{V}_{ee} + \hat{V}_{\text{ext}} | \Psi \rangle \\
 &= T[\rho] + V_{ee}[\rho] + \int d\mathbf{r} \rho(\mathbf{r}) V_{\text{ext}}(\mathbf{r}) \\
 &\equiv F[\rho] + \int d\mathbf{r} \rho(\mathbf{r}) V_{\text{ext}}(\mathbf{r})
 \end{aligned} \tag{2.2}$$

where Ψ is the wave function of the system and $\rho(\mathbf{r})$ is the electron density defined as expectation of the electron density operator $\hat{\rho}(\mathbf{r}) \equiv \sum_{i=1}^N \delta(\mathbf{r} - \mathbf{r}_i)$:

$$\begin{aligned}
 \rho(\mathbf{r}) &= \langle \Psi | \hat{\rho}(\mathbf{r}) | \Psi \rangle \\
 &= \sum_{i=1}^N \int d\xi_1 d\xi_2 \dots d\xi_{i-1} d\sigma_i d\xi_{i+1} \dots d\xi_N |\Psi(\xi_1, \xi_2, \dots, \xi_{i-1}, \xi_i, \xi_{i+1}, \dots, \xi_N)|^2
 \end{aligned} \tag{2.3}$$

where the coordinate $\xi_i = (\mathbf{r}_i, \sigma_i)$ includes orbital and spin coordinate. The functional $F[\rho]$ is universal for all electron system with the density $\rho(\mathbf{r})$ because the term does not contain the external potential. When the $F[\rho]$ was determined, we obtain the exact ground state energy and density by minimizing the total energy $E[\rho]$ with respect to variations in the electron density as follows:

$$\begin{aligned}
 \delta \left\{ E[\rho] - \mu \left[\int d\mathbf{r} \rho(\mathbf{r}) - N \right] \right\} &= 0 \\
 \rightarrow \frac{\delta E[\rho]}{\delta \rho(\mathbf{r})} - \mu \int d\mathbf{r}' \frac{\delta \rho(\mathbf{r}')}{\delta \rho(\mathbf{r})} &= 0 \\
 \frac{\delta F[\rho]}{\delta \rho(\mathbf{r})} + V_{\text{ext}}(\mathbf{r}) - \mu &= 0
 \end{aligned} \tag{2.4}$$

where μ is a Lagrange multiplier associated with the total electron number corresponding with the chemical potential.

2.1.2 Kohn-Sham Equation

Hohenberg and Kohn showed that the ground state energy of many-body systems can be described by the electron density as a basic variable. For the practical application of the theorem, it is mandatory to derive a self-consistent equation to provide the ground state electron density. Kohn and Sham provided a set of self-consistent one-electron equation [50]. They assumed that the ground state density of the interacting electron system is replaced by the one of an auxiliary system of independent electrons. The density of the auxiliary system is written by using the one-electron states $\psi_i^\sigma(\mathbf{r})$ for each

spin variable σ

$$\rho(\mathbf{r}) = \sum_{\sigma} \rho^{\sigma}(\mathbf{r}) = \sum_{\sigma} \sum_{i=1}^{N^{\sigma}} |\psi_i^{\sigma}(\mathbf{r})|^2. \quad (2.5)$$

Additionally, the kinetic energy of the auxiliary system is written as

$$T_s = -\frac{1}{2} \sum_{\sigma} \sum_{i=1}^{N^{\sigma}} \langle \psi_i^{\sigma} | \nabla^2 | \psi_i^{\sigma} \rangle = \frac{1}{2} \sum_{\sigma} \sum_{i=1}^{N^{\sigma}} \int d\mathbf{r} |\nabla \psi_i^{\sigma}(\mathbf{r})|^2 \quad (2.6)$$

and the classical Coulomb's interaction energy is defined as

$$V_H[\rho] = \frac{1}{2} \int d\mathbf{r} d\mathbf{r}' \frac{\rho(\mathbf{r})\rho(\mathbf{r}')}{|\mathbf{r} - \mathbf{r}'|}. \quad (2.7)$$

Thus, by the above definitions, the ground state energy functional Eq. (2.2) can be rewritten as

$$E[\{\rho^{\sigma}\}] = T_s[\{\rho^{\sigma}\}] + V_H[\rho] + E_{xc}[\{\rho^{\sigma}\}] + \int d\mathbf{r} \rho(\mathbf{r}) V_{\text{ext}}(\mathbf{r}) \quad (2.8)$$

where all many-body effects are incorporated into exchange-correlation energy E_{xc} :

$$\begin{aligned} E_{xc}[\{\rho^{\sigma}\}] &\equiv T[\{\rho^{\sigma}\}] - T_s[\{\rho^{\sigma}\}] + V_{ee}[\{\rho^{\sigma}\}] - V_H[\rho] \\ &= F[\{\rho^{\sigma}\}] - T_s[\{\rho^{\sigma}\}] - V_H[\rho]. \end{aligned} \quad (2.9)$$

E_{xc} is the functional of non-classical term of V_{ee} and the difference between T and T_s which is associated with the many-body effects in the kinetic energy.

To get the ground state energy, the energy functional E is minimized by taking the functional derivative with respect to the one-electron states under the normalization condition $\langle \psi_i^{\sigma} | \psi_i^{\sigma} \rangle = 1$,

$$\begin{aligned} 0 &= \frac{\delta}{\delta \psi_i^{\sigma*}(\mathbf{r})} \left[E - \sum_{j,\sigma'} \varepsilon_j^{\sigma'} \left(\int d\mathbf{r}' \psi_j^{\sigma'*}(\mathbf{r}') \psi_j^{\sigma'}(\mathbf{r}') - 1 \right) \right] \\ &= \frac{\delta T_s}{\delta \psi_i^{\sigma*}(\mathbf{r})} + \left[\frac{\delta V_H}{\delta \rho^{\sigma}(\mathbf{r})} + \frac{\delta E_{xc}}{\delta \rho^{\sigma}(\mathbf{r})} + \int d\mathbf{r}' \delta^3(\mathbf{r}' - \mathbf{r}) V_{\text{ext}}(\mathbf{r}') \right] \frac{\delta \rho^{\sigma}(\mathbf{r})}{\delta \psi_i^{\sigma*}(\mathbf{r})} - \varepsilon_i^{\sigma} \psi_i^{\sigma}(\mathbf{r}) \\ &= \left(-\frac{1}{2} \nabla^2 + \int d\mathbf{r}' \frac{\rho(\mathbf{r}')}{|\mathbf{r} - \mathbf{r}'|} + \frac{\delta E_{xc}}{\delta \rho^{\sigma}(\mathbf{r})} + V_{\text{ext}}(\mathbf{r}) - \varepsilon_i^{\sigma} \right) \psi_i^{\sigma}(\mathbf{r}). \end{aligned} \quad (2.10)$$

The derivative brings the one-body Schrödinger-like equation,

$$\hat{H}^{\sigma} \psi_i^{\sigma}(\mathbf{r}) = \varepsilon_i^{\sigma} \psi_i^{\sigma}(\mathbf{r}) \quad (2.11)$$

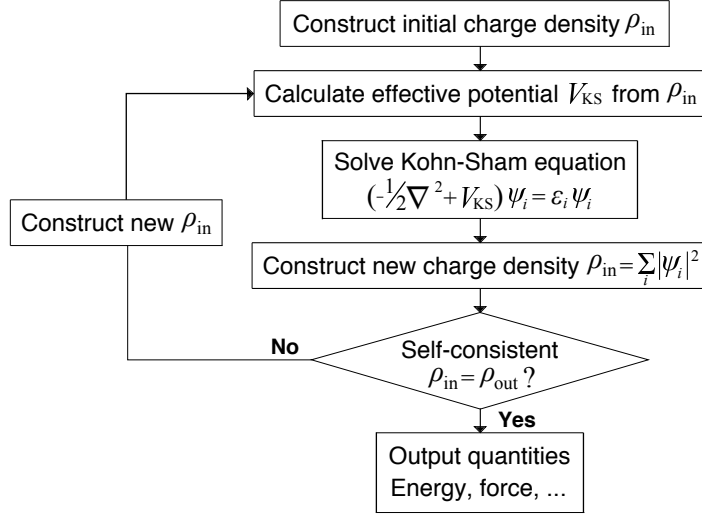


FIGURE 2.1: Flow diagram to solve the Kohn-Sham equations.

where ε_i^σ is an energy eigenvalue of each state $\psi_i^\sigma(\mathbf{r})$ and \hat{H}^σ is a effective hamiltonian

$$\begin{aligned}
 \hat{H}^\sigma &= -\frac{1}{2} \nabla^2 + \int d\mathbf{r}' \frac{\rho(\mathbf{r}')}{|\mathbf{r} - \mathbf{r}'|} + \frac{\delta E_{xc}}{\delta \rho^\sigma(\mathbf{r})} + V_{\text{ext}}(\mathbf{r}) \\
 &\equiv -\frac{1}{2} \nabla^2 + \int d\mathbf{r}' \frac{\rho(\mathbf{r}')}{|\mathbf{r} - \mathbf{r}'|} + V_{xc}^\sigma(\mathbf{r}) + V_{\text{ext}}(\mathbf{r}) \\
 &\equiv -\frac{1}{2} \nabla^2 + V_{KS}^\sigma(\mathbf{r})
 \end{aligned} \tag{2.12}$$

where $V_{xc}^\sigma(\mathbf{r})$ is a exchange-correlation potential and $V_{KS}^\sigma(\mathbf{r})$ is a Kohn-Sham potential. The Kohn-Sham equation Eq. (2.11) is the non linear equation for independent particles moving in the effective potential $V_{KS}^\sigma(\mathbf{r})$, because $V_{KS}^\sigma(\mathbf{r})$ is the functional of $\rho(\mathbf{r})$ which is obtained by solving the equation itself. The equation is independent of any approximation to the exchange-correlation energy E_{xc} . Thus, the exact ground state energy and density in the many-body system are determined by solving the Kohn-Sham equation with the exact E_{xc} . A procedure for solving the Kohn-Sham equation is shown in Fig. 2.1. We solve the Kohn-Sham equation iteratively until the input $\rho_{in}(\mathbf{r})$ accords with the updated $\rho_{out}(\mathbf{r})$.

2.2 Exchange-correlation Energy Functional

To solve the Kohn-Sham equation of atoms, molecules, and solids, we have to introduce an explicit form of the exchange-correlation energy E_{xc} . In this section, representative approximations for E_{xc} are introduced.

2.2.1 Local Density Approximation

The local density approximation (LDA) is the simplest form of the exchange-correlation energy which is constructed by assuming that the exchange-correlation energy per electron at the position \mathbf{r} is equivalent to that in a locally homogeneous electron gas with the same density $\varepsilon_{xc}^{\text{homo}}(\rho(\mathbf{r}))$ [54, 55]. Thus, the exchange-correlation energy E_{xc} is written as

$$\begin{aligned} E_{xc}[\rho] &= \int d\mathbf{r} \varepsilon_{xc}^{\text{homo}}(\rho(\mathbf{r})) \rho(\mathbf{r}) \\ &= \int d\mathbf{r} \left[\varepsilon_x^{\text{homo}}(\rho(\mathbf{r})) + \varepsilon_c^{\text{homo}}(\rho(\mathbf{r})) \right] \rho(\mathbf{r}) \end{aligned} \quad (2.13)$$

where $\varepsilon_x^{\text{homo}}$ and $\varepsilon_c^{\text{homo}}$ are the exchange and correlation energy, respectively. Based on results for the homogeneous electron gas, the $\varepsilon_x^{\text{homo}}$ is calculated exactly: $\varepsilon_x^{\text{homo}} = -3k_F/4\pi$ where $k_F = (3\pi^2\rho(\mathbf{r}))^{1/3}$, whereas the $\varepsilon_c^{\text{homo}}$ is parametrized from the Quantum Monte Carlo method on the homogeneous gas [55]. Although the assumption is simple, LDA is widely used and provide accurate results for many systems. One reason of this success is that the LDA exchange-correlation hole satisfies the charge-conservation sum rule [56, 57]. Additionally, the detailed shape of the hole is not required because the exchange-correlation energy depends only on a spherical average of the hole.

2.2.2 Generalized Gradient Approximation

Although LDA well reproduces the physical properties of atoms, molecules, and solids, it is insufficient to describe the system where the electron density varies rapidly over a small region of space because the E_{xc} is evaluated by the homogeneous electron gas. Indeed, LDA could not reproduce the magnetic state of metals containing d -electron. Furthermore, LDA is also known to overestimate the interatomic interaction, leading to the underestimation of the interatomic spacing. To overcome the shortcoming, it is natural to take the gradient correction into account. Thus the exchange correlation potential of the generalized gradient approximation (GGA) is formally expressed

$$E_{xc}[\rho] = \int d\mathbf{r} \rho(\mathbf{r}) \varepsilon_{xc}(\rho(\mathbf{r}), |\nabla\rho(\mathbf{r})|). \quad (2.14)$$

Similar to the LDA, the $E_{xc}[\rho]$ for the GGA is decomposed into exchange and correlation functional. For the ε_{xc} , functional forms of the Perdew-Wang (PW91) [58] and that of the Perdew-Burke-Ernzerhof (PBE) [59] are widely used. The GGA functionals generally improve magnetic properties of transition metals and bond length of molecules and solids.

van der Waals Interaction

GGA is not able to describe the weak dispersive interaction (van der Waals interaction) because of the rapid decrease in the electron density [60]. Thus, to evaluate van der Waals (vdW) interactions, Cooper proposed a GGA exchange functional containing

vdW correlation [61]. In the conventional GGA, the exchange energy E_x is written as

$$E_x[\rho] = \int d\mathbf{r} \rho(\mathbf{r}) \varepsilon_x^{\text{homo}}(\rho) F_x(s) \quad (2.15)$$

where $s = |\nabla\rho|/(2k_F\rho)$ is a dimensionless reduced density gradient and $F_x(s)$ is an exchange enhancement factor which is calculated analytically [62, 63]. The second-order density gradient expansion of the factor is

$$F_x^{\text{GEA}}(s) = 1 + \mu s^2 \quad (2.16)$$

where $\mu = 0.0864$ which is used in PW86 [64]. To incorporate vdW correction in the formula of the vdW density functional [65, 66], the functional $F_x(s)$ is replaced as

$$F_x(s) = 1 + \mu s^2 e^{-\alpha s^2} + \beta \left(1 - e^{-\alpha s^2/2}\right) \quad (2.17)$$

where $\mu = 0.0617$, $\beta = 1.245$, and $\alpha = 0.0483$, which are determined by matching $F_x(s)$ to the $F_x^{\text{GEA}}(s)$ in the slowly varying/high-density limit and asymptotically approaching to the upper bound of the exchange enhancement factor in revPBE [67], leading to the reasonable exchange functional to express vdW interaction [68].

2.3 Plane-wave Basis Set

To calculate the Kohn-Sham equation, one-body wave function should be expressed in terms of an appropriate basis set. In this thesis, the plane-wave basis set is adopted to expand valence wave functions

$$\psi_{i,\mathbf{k}}(\mathbf{r}) = \frac{1}{\sqrt{\Omega}} \sum_{\mathbf{K}} C_{i,\mathbf{k}}(\mathbf{K}) e^{i(\mathbf{k}+\mathbf{K})\cdot\mathbf{r}} \quad (2.18)$$

where Ω is the volume of the unit cell and \mathbf{K} is the reciprocal lattice vector defined by $\mathbf{K}\cdot\mathbf{l} = 2\pi n$ for a lattice vector \mathbf{l} of the system and an integer n . Although the orthonormality is guaranteed by taking \mathbf{K} summation up to infinity, it is able to truncate the sum up to a particular cutoff energy, because the coefficients $C_{i,\mathbf{k}}(\mathbf{K})$ with small kinetic energy $|\mathbf{k} + \mathbf{K}|^2/2$ are practically more dominant than those with large kinetic energy. Note that the cutoff energy determines the computational accuracy and cost.

The plane-wave basis set is useful for describing electron states of solids, because the plane-waves are origin-less functions which do not depend on the positions of the nuclei. Another advantage of the plane-wave basis set is that it can reproduce the delocalized state of which distribution is dislodged from nuclei. By substituting the plane-wave basis set Eq. (2.18) into the Kohn-Sham equation Eq. (2.10), we can get a secular equation

of the coefficient $C_{i,\mathbf{k}}(\mathbf{K})$:

$$\begin{aligned} \epsilon_i C_{i,\mathbf{k}}(\mathbf{K}) = & \sum_{\mathbf{K}'} \left[\frac{|\mathbf{k} + \mathbf{K}'|^2}{2} \delta_{\mathbf{K}\mathbf{K}'} \right. \\ & \left. + \frac{1}{\Omega} \int d\mathbf{r} \left(\int d\mathbf{r}' \frac{\rho(\mathbf{r}')}{|\mathbf{r} - \mathbf{r}'|} + V_{\text{xc}}(\mathbf{r}) + V_{\text{ext}}(\mathbf{r}) \right) e^{-i(\mathbf{K}' - \mathbf{K}) \cdot \mathbf{r}} \right] C_{i,\mathbf{k}}(\mathbf{K}'). \end{aligned} \quad (2.19)$$

Therefore, the differential equation of $\psi_{i,\mathbf{k}}$ turns into the diagonalization of matrix consisting of the kinetic energy and effective potential. Note that the matrix size depends on the cutoff energy. In particular, to expand the wave function associated with core electrons, a large cutoff energy is required for reproducing the wave function rapidly oscillating in the core region.

2.4 Pseudopotential

In this section, we describe the pseudopotential approach to reduce the computational cost arising from the large cutoff energy of plane-wave expansion for describing the rapid oscillation of wave functions near the nuclei. An idea of pseudopotential is that the real potential arising from core electrons and nuclei is replaced by an adequate pseudopotential providing the same environment for valence electrons, because the most of physical and chemical properties of matters are determined by valence electrons. In this section, we briefly explain the norm-conserving pseudopotential (NCPP) and then we explain ultrasoft pseudopotential (USPP) used in this thesis, which are known to be representative ab initio pseudopotentials to date.

The Pseudo Potential Idea

We start with the Schrödinger equation of an atom with core states $|\psi_c\rangle$ and valence states $|\psi_v\rangle$

$$\hat{H}|\psi_i\rangle = E_i|\psi_i\rangle \quad i = c \text{ and } v. \quad (2.20)$$

With a smooth (nodeless) wave function for the valence state $|\psi_v^{\text{P}}\rangle$ which is pseudo wave function, the valence state $|\psi_v\rangle$ is divided into the smooth part and the localized part:

$$|\psi_v\rangle = |\psi_v^{\text{P}}\rangle - \sum_c |\psi_c\rangle \langle \psi_c | \psi_v^{\text{P}} \rangle. \quad (2.21)$$

The pseudo wave function satisfies the following Schrödinger-like equation with modified potential

$$\hat{H}|\psi_v^{\text{P}}\rangle = E_v|\psi_v^{\text{P}}\rangle + \sum_c (E_c - E_v) |\psi_c\rangle \langle \psi_c | \psi_v^{\text{P}} \rangle. \quad (2.22)$$

Thus

$$(\hat{T} + V^{\text{PP}})|\psi_v^{\text{P}}\rangle = E_v|\psi_v^{\text{P}}\rangle \quad (2.23)$$

where V^{PP} is pseudopotential defined using the true potential V

$$V^{\text{PP}} = V - \sum_c (E_c - E_v) |\psi_c\rangle \quad (2.24)$$

The second term in Eq. (2.22) corresponds with the non-local repulsive potential, making the V^{PP} weaker than V in the vicinity of core region, so that the $|\psi_v^{\text{P}}\rangle$ is the smooth and nodeless function in the core region.

2.4.1 Norm-conserving Pseudopotential

Norm-conserving pseudopotential (NCP) is a nonempirical pseudopotential relying on ab initio calculations. To construct the norm-conserving pseudopotential, following four conditions are required [69–72]:

1. All-electron (AE) and the valence pseudo eigenvalues must be equal each other for the chosen core reference configuration.
2. Valence pseudo wave function must be equal to the AE wave function beyond a chosen cutoff radius r_c .

$$\phi_l^{\text{NP}}(r) = \phi_l^{\text{AE}}(r) \quad \text{if } r \geq r_c \quad (2.25)$$

where $\phi_l^{\text{NP}}(r)$ and $\phi_l^{\text{AE}}(r)$ are the radial part of the pseudo and AE wave function with angular momentum l , respectively.

These two conditions indicate that NCP is the same as AE potential beyond r_c where is important domain for bonding.

3. The integrated charge for each wave function must be equal inside r_c .

$$\int_0^{r_c} dr r^2 |\phi_l^{\text{NP}}(r)|^2 = \int_0^{r_c} dr r^2 |\phi_l^{\text{AE}}(r)|^2 \quad (2.26)$$

4. The valence pseudo wave function should be a nodeless function inside r_c .

In addition, the first energy derivative of the logarithmic derivatives of pseudo and AE wave functions agrees at r_c , which is required for the transferability of the pseudopotential:

$$\left. \frac{\partial}{\partial \varepsilon'} \chi_l(r_c, \varepsilon') \right|_{\varepsilon'=\varepsilon} = \frac{-2}{[r_c \phi_l(r_c, \varepsilon)]^2} \int_0^{r_c} dr r^2 \phi_l(r, \varepsilon)^2 \quad (2.27)$$

where $\chi_l(r, \varepsilon) = d \ln(r \phi_l(r, \varepsilon)) / dr$. Since the $\chi_l(r_c, \varepsilon)$ determines scattering phase shift, Eq. (2.27) also implies the pseudopotential has the same scattering property as that of the AE potential within the first order in energy around the chosen energy. Thus, the NCP describes the physics associated with the valence electrons in any systems.

Semi-local Pseudopotentials

Because the phase shifts produced by the ionic core depend on the angular momentum state, the pseudopotential intrinsically possesses non-locality as

$$\hat{V} = \sum_{lm} |lm\rangle V_l(r) \langle lm| \quad (2.28)$$

where $|lm\rangle$ is the spherical harmonic and $V_l(r)$ is the pseudopotential for angular momentum l . By separating the potential V_l into local term V_{loc} and non-local term δV_l , the potential is expressed as

$$\hat{V} = V_{loc}(r) + \sum_{lm} |lm\rangle \delta V_l(r) \langle lm| \quad (2.29)$$

where V_{loc} is a long-range potential and behaving like $-Z_v e^2/r$ for large r where Z_v is the number of valence electrons, and δV_l is a short-ranged and vanishing beyond the core radius r_c , because the pseudopotential is the same as the l -independent AE potential beyond the core radius r_c .

2.4.2 Ultrasoft Pseudopotential

Although NCPP substantially decreases computational cost by introducing the smooth nodeless pseudo wave function, for elements with strongly localized states, NCPP still requires a large plane-wave basis set to expand the valence wave functions. The ultrasoft pseudopotential (USPP) is softer than the NCPP without imposing the norm-conserving condition, leading to further reducing a plane-wave basis set [73, 74].

Here we briefly explain a formalism of USPP. In some reference configurations, an AE calculation is carried out on a free atom. Then the Schrödinger equation is written as

$$\left(-\frac{1}{2} \nabla^2 + V^{AE} \right) |\psi_s^{AE}\rangle = \varepsilon_s |\psi_s^{AE}\rangle \quad (2.30)$$

where V^{AE} and ψ_s^{AE} are the AE potential and AE wave function with the composite index $s = (nlm)$, respectively. For each angular momentum, a set of reference energies ε_s is chosen. Next, a smooth local potential $V_{loc}(r)$ and pseudo wave functions $\psi_s^P(r)$ are created which correspond with real them outside r_c^{loc} and r_c , respectively.

$$V_{loc}(r) = V^{AE}(r) \quad (r \geq r_c^{loc}) \quad (2.31)$$

$$\psi_s^P(r) = \psi_s^{AE}(r) \quad (r \geq r_c) \quad (2.32)$$

Then, new orbitals are defined as

$$|\chi_s\rangle \equiv \left[\varepsilon_s - \left(-\frac{1}{2} \nabla^2 + V_{loc} \right) \right] |\psi_s^P\rangle \quad (2.33)$$

which vanishes at and beyond radius R , where $V_{loc} = V^{AE}$ and $\psi_s^P = \psi_s^{AE}$. An auxiliary matrix of inner products is defined as

$$B_{s,s'} \equiv \langle \psi_s^P | \chi_{s'} \rangle. \quad (2.34)$$

The set of projectors, $|\beta_s\rangle$, which are necessary to define the non-local part of the potential, are formed

$$|\beta_s\rangle \equiv \sum_{s'} B_{s',s}^{-1} |\chi_{s'}\rangle \quad (2.35)$$

which is dual to $|\psi_s^P\rangle$: $\langle \beta_s | \psi_{s'}^P \rangle = \delta_{s,s'}$. Then, define matrix $D_{s,s'}$

$$D_{s,s'} = B_{s,s'} + \varepsilon_{s'} Q_{s,s'} \quad (2.36)$$

using deficit charge $Q_{s,s'}$ written as

$$\begin{aligned} Q_{s,s'} &= \int_0^R d\mathbf{r} \psi_s^{AE}(\mathbf{r})^* \psi_{s'}^{AE}(\mathbf{r}) - \int_0^R d\mathbf{r} \psi_s^P(\mathbf{r})^* \psi_{s'}^P(\mathbf{r}) \\ &\equiv \int_0^R d\mathbf{r} \Delta Q_{s,s'}(\mathbf{r}) \end{aligned} \quad (2.37)$$

where $\Delta Q_{s,s'}$ is an augmentation function which is localized in the core region. The $D_{s,s'}$ is a Hermitian matrix, although the matrix $B_{s,s'}$ is Hermitian only if the norm is conserved ($Q_{s,s'} = 0$). With all these descriptions, it is straightforward to verify that the ψ_s^P obeys the secular equation:

$$\left(-\frac{1}{2} \nabla^2 + V_{loc} + \delta \hat{V}_{NL}^{US} \right) |\psi_s^P\rangle = \varepsilon_s \hat{S} |\psi_s^P\rangle \quad (2.38)$$

where an overlap matrix \hat{S} is defined as

$$\hat{S} \equiv \hat{\mathbf{1}} + \sum_{s,s'} Q_{s,s'} |\beta_s\rangle \langle \beta_{s'}| \quad (2.39)$$

which gives the S-orthonormality of ψ_i^P : $\langle \psi_i^P | \hat{S} | \psi_j^P \rangle = \delta_{i,j}$, and $\delta \hat{V}_{NL}^{US}$ is a non-local potential that operates on the ψ_s^P expressed as

$$\delta \hat{V}_{NL}^{US} \equiv \sum_{s,s'} |\beta_s\rangle D_{s,s'} \langle \beta_{s'}|. \quad (2.40)$$

The potential V_{loc} and $\delta \hat{V}_{NL}^{US}$ include the interaction among the valence electron states. We therefore subtract the Hartree potential V_H^{PP} and exchange-correlation potential V_{xc}^{PP} calculated only for the valence pseudo wave function, leading to the bare ion pseudopotential which is transferable to different environment.

$$V_{loc,ion}(\mathbf{r}) \equiv V_{loc}(\mathbf{r}) - [V_H^{PP}(\mathbf{r}) + V_{xc}^{PP}(\mathbf{r})] \quad (2.41)$$

$$D_{s,s'}^{(0)} \equiv D_{s,s'} - \int d\mathbf{r} V_{loc}(\mathbf{r}) \Delta Q_{s,s'}(\mathbf{r}) \quad (2.42)$$

Then, we finally obtain the USPP as

$$V_{ion}^{US}(\mathbf{r}) = V_{loc,ion}(\mathbf{r}) + \sum_{s,s'} |\beta_s\rangle D_{s,s'}^{(0)} \langle \beta_{s'}|. \quad (2.43)$$

In this formalism, we introduce the deficit charge $Q_{s,s'}$ and the overlap matrix \hat{S} to maintain the desired accuracy without the norm-conserving condition. By using $Q_{s,s'}$, the valence electron density $\rho_v(\mathbf{r})$ is defined to be

$$\rho_v(\mathbf{r}) = \sum_i |\psi_i^P(\mathbf{r})|^2 + \sum_i \sum_{s,s'} \langle \psi_i^P | \beta_s^P \rangle \Delta Q_{s,s'}(\mathbf{r}) \langle \beta_{s'}^P | \psi_i^P \rangle \quad (2.44)$$

where the valence electron density has a smooth part and a sharp part, and the integral of the density gives the correct number of valence electrons. Note that the USPP expresses the same phase shift as that of the real potential. Thus, by increasing the number of the reference energy, the scattering property of the USPP coincides with the AE one in a wide energy range.

2.5 Effective Screening Medium Method

In this section, we explain the effective screening medium (ESM) method, which allows to calculate the surfaces, slabs, and molecules under particular boundary conditions along one of three bases within the framework of the DFT using plane-wave basis set (DFT-PW). Let us consider an isolated slab with electrostatic polarity normal to its surface. In the DFT-PW scheme, we usually take a large cell parameter normal to the slab to exclude unphysical interaction with the periodic images. However, unfortunately, a dipole-dipole interaction with the image cells could not omit, even though we consider very large cell parameter, because the classical electrostatic interaction is a long-range interaction. The ESM method [75, 76] could overcome the difficulty by considering the ESM which is the semi-infinite continuous media characterized by only relative permittivity $\epsilon(\mathbf{r})$ at two cell boundaries [Fig. 2.2]. In this isolated slab geometry, the Poisson's equation is solved in the whole space under various boundary conditions normal to the slab surface with the aid of the Green's function technique, while the Kohn-Sham equation is solved in a cell with a finite length normal to the surface under the periodic boundary condition (PBC). The models are restricted to a situation where the surface and the electrode are electronically disconnected and the electrons are confined to the region from $-z_u$ to z_u . The separated treatment of the Poisson and the Kohn-Sham equations minimizes the modification of the DFT-PW scheme, and gives the models the possibility of application for various experimental situations.

Starting with the total energy as a functional of the electron density and potential

$$E[\rho_e, V] = T[\rho_e] + E_{xc}[\rho_e] + \int d\mathbf{r} \left[-\frac{\epsilon(\mathbf{r})}{8\pi} |\nabla V(\mathbf{r})|^2 + (\rho_e(\mathbf{r}) + \rho_i(\mathbf{r})) V(\mathbf{r}) \right] \quad (2.45)$$

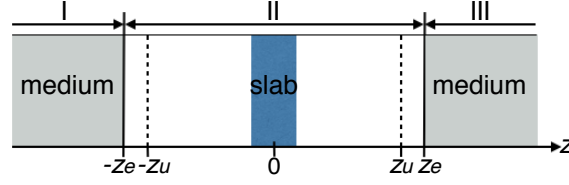


FIGURE 2.2: ESM model in which a slab model is sandwiched by semi-infinite media. z_u and z_e are correspond with the cell boundary for repeated slab calculations and the interface between the vacuum and the medium, respectively.

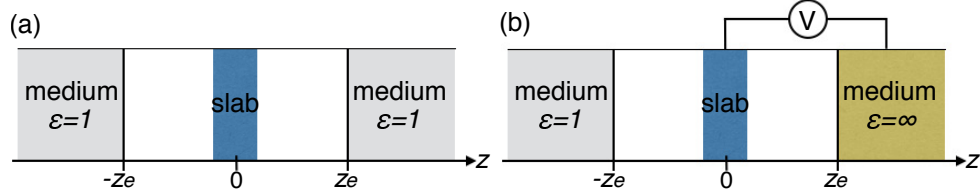


FIGURE 2.3: ESM models with representative boundary condition, which show (a) a slab located in vacuum and (b) a FET model.

where $\rho_e(\mathbf{r})$, $\rho_i(\mathbf{r})$, $V(\mathbf{r})$, and $\epsilon(\mathbf{r})$ are the electron charge density, the nuclear charge density, the electrostatic potential, and the relative permittivity of ESM, respectively. Furthermore, T and E_{xc} are a kinetic and exchange-correlation energy functionals of $\rho_e(\mathbf{r})$, respectively. For simplicity, an entropic term of the electrons and a classical charge density are omitted. The Poisson's equation is written as

$$\nabla[\epsilon(\mathbf{r})\nabla]V(\mathbf{r}) = -4\pi\rho_{tot}(\mathbf{r}) \quad (2.46)$$

where ρ_{tot} is the sum of ρ_i and ρ_e . Eq. (2.46) is rewritten using Green's function:

$$\nabla[\epsilon(\mathbf{r})\nabla]G(\mathbf{r}, \mathbf{r}') = -4\pi\delta(\mathbf{r} - \mathbf{r}'). \quad (2.47)$$

The electrostatic potential is expressed as

$$V(\mathbf{r}) = \int d\mathbf{r}' G(\mathbf{r}, \mathbf{r}') \rho_{tot}(\mathbf{r}'). \quad (2.48)$$

Using the Green's function, the total energy functional Eq. (2.45) is rewritten as

$$\begin{aligned} E[\rho_e] &= T[\rho_e] + E_{xc}[\rho_e] + \frac{1}{2} \int d\mathbf{r} d\mathbf{r}' \rho_e(\mathbf{r}) G(\mathbf{r}, \mathbf{r}') \rho_e(\mathbf{r}') \\ &+ \int d\mathbf{r} d\mathbf{r}' \rho_e(\mathbf{r}) G(\mathbf{r}, \mathbf{r}') \rho_i(\mathbf{r}') + \frac{1}{2} \int d\mathbf{r} d\mathbf{r}' \rho_i(\mathbf{r}) G(\mathbf{r}, \mathbf{r}') \rho_i(\mathbf{r}') \end{aligned} \quad (2.49)$$

where the third, fourth, and fifth terms represent the Hartree, electron-ion interaction, and ion-ion interaction energies, respectively. By taking the density variation, the Kohn-Sham equation is obtained from the total energy functional.

To solve the Green's function of the Poisson's equation analytically, the periodic boundary condition (PBC) is imposed in x - y plane while an open boundary condition is imposed normal to the plane. Under the conditions, the Poisson's equations Eq. (2.46)

and Eq. (2.47) are rewritten by Laue representation as follows

$$\left(\partial_z[\epsilon(z)\partial_z] - \epsilon(z)k_{\parallel}^2\right) V(\mathbf{k}_{\parallel}, z) = -4\pi\rho_{tot}(\mathbf{k}_{\parallel}, z) \quad (2.50)$$

$$\left(\partial_z[\epsilon(z)\partial_z] - \epsilon(z)k_{\parallel}^2\right) G(\mathbf{k}_{\parallel}, z, z') = -4\pi\delta(z - z') \quad (2.51)$$

where \mathbf{k}_{\parallel} is wave vector on x - y plane and k_{\parallel} is the absolute value of the \mathbf{k}_{\parallel} . The representative model dependent boundary conditions are

$$(a) \quad \partial_z V(\mathbf{k}_{\parallel}, z)|_{z=\pm\infty} = 0, \quad \epsilon(z) = 1 \quad (2.52)$$

$$(b) \quad \begin{cases} V(\mathbf{k}_{\parallel}, z)|_{z=z_e} = 0 \\ \partial_z V(\mathbf{k}_{\parallel}, z)|_{z=-\infty} = 0, \end{cases} \quad \epsilon(z) = \begin{cases} 1 & (\text{if } z \leq z_e) \\ \infty & (\text{if } z \geq z_e). \end{cases} \quad (2.53)$$

The first condition corresponds to the slab located in vacuum [Fig. 2.3(a)], in which the electrostatic potential is obtained in reference to the vacuum level. Using the condition, we can calculate the slabs with surface dipole and work function of polar surface without considering the additional corrections. The second condition is a field-effect transistor (FET) model, in which the metal electrode is located at $+z_e$ while the vacuum is located at the other cell boundary. We can inject carriers into the slabs under the condition [Fig. 2.3(b)]. The model-depending green function can be obtained by solving the Poisson's equation under each condition with the aid of a Sturm-Liouville equation.

Chapter 3

Graphene Adsorbing Al_x Nanoparticles

In this Chapter, we discuss the effect of Al nanoparticles on carrier accumulation in graphene by an external electric field. Furthermore, we also investigate geometric structures of Al nanoparticles on graphene under the electric field.

3.1 Introduction

Graphene has been keeping a premier position not only in low-dimensional sciences but also in nanoscale technologies due to its unique structural and electronic properties [4, 10, 44, 77]. Pairs of linear dispersion bands at six corners of the Brillouin zone cause the unusual Hall effect [14, 78] and a remarkable carrier mobility [79] of 200,000 cm^2/Vs , which make graphene an emerging material for high-speed switching electronic devices [80]. In addition to its intrinsic unique electronic properties, graphene exhibits further variation in its electronic structure by forming hybrid structures with foreign materials and the external environment [23, 29, 81, 82]. It has been demonstrated that graphene does not possess the zero-gap semiconducting electronic structure but quadratic dispersion band with a finite energy gap which depends on the surface morphology when graphene is adsorbed on insulating substrates [83–86], metal surfaces [87], and defective graphene layers [48], owing to the modulation of the electrostatic potential of graphene by foreign materials. Atoms and molecules adsorbed on the graphene also modulate the Dirac cone of graphene by covalent and van der Waals interaction between adsorbates and graphene [88, 89]. Besides, an external electric field also affects the electronic structure of graphene and its hybrids [41, 47, 90, 91]. Therefore, for the fundamental and applied sciences of graphene, it is mandatory to precisely control their electronic structure by external conditions, such as the chemical modification, atom/molecule doping, and the external electric field. In particular, the band gap engineering and the Fermi level tuning are highly important for the fundamental study and application of graphene, because graphene inherently possesses hybrid structures with foreign materials. Although the carrier accumulation in pristine graphene and graphite under an

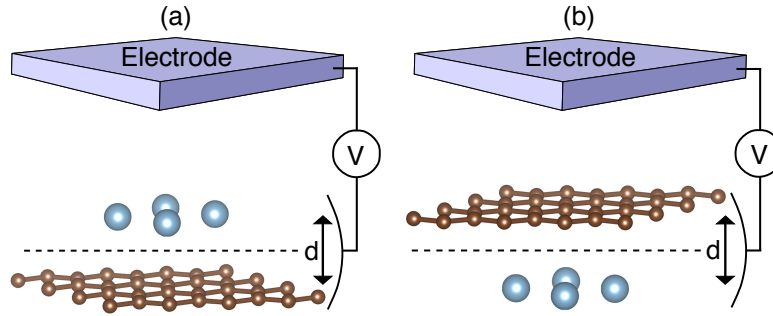


FIGURE 3.1: Structural models of Al nanoparticles adsorbed on graphene with the FET structure with the (a) electrode-Al-graphene and (b) electrode-graphene-Al arrangements. Large and small balls denote Al and C atoms, respectively. Slabs situated above the hybrid consisting of graphene and Al nanoparticles denote the counter electrodes, which are simulated by the ESM.

external electric field has been steadily elucidated [47, 92], the microscopic mechanism of the carrier injection into graphene under such hybrid structures is not elucidated yet. In particular, it is uncertain whether the foreign materials prevent or assist the carrier injection into graphene in the hybrid structures.

In this Chapter, we show the electronic and geometric structures of Al nanoparticles adsorbed on graphene under excess electron or hole injected by a counter electrode for providing the theoretical insight into the fundamental properties of graphene-based FET containing metallic impurities.

3.2 Computational Parameters and Structural Models

We consider the graphene FET in which Al nanoparticles are physisorbed on the graphene surfaces with two different adsorption arrangements with respect to the electrode [Fig. 3.1]. We consider Al_4 and Al_3 nanoparticles as representative impurity nanoparticles in the graphene FET, which are adsorbed on graphene per 4×4 lateral periodicity in parallel arrangement. Al_4 and Al_3 nanoparticles have triangular and square conformations, respectively, of which molecular plane is parallel to graphene, enhancing the interaction between the nanoparticles and graphene. To investigate the geometric and electronic structures of graphene with metal nanoparticles under electron and hole injection, we adopted the ESM method to solve the Poisson's equation under a boundary condition in which a planar metal electrode with an infinite relative permittivity and a half-infinite vacuum are situated at two-cell boundaries parallel to the graphene layer [Fig. 3.1] [75]. Electrons and holes were injected by the planar counter gate electrode situated at the cell boundary dislodged by 6.35 \AA from the center of graphene and Al nanoparticles. We perform first-principles total energy calculations combined with the ESM method within the framework of the DFT [49, 50] (STATE package [93]). To express the exchange correlation potential among the interacting electrons, the LDA was applied with the Perdew–Wang functional form [58], since the LDA is known to qualitatively express weak interactions in carbon nanomaterials [94]. We used USPP generated using the

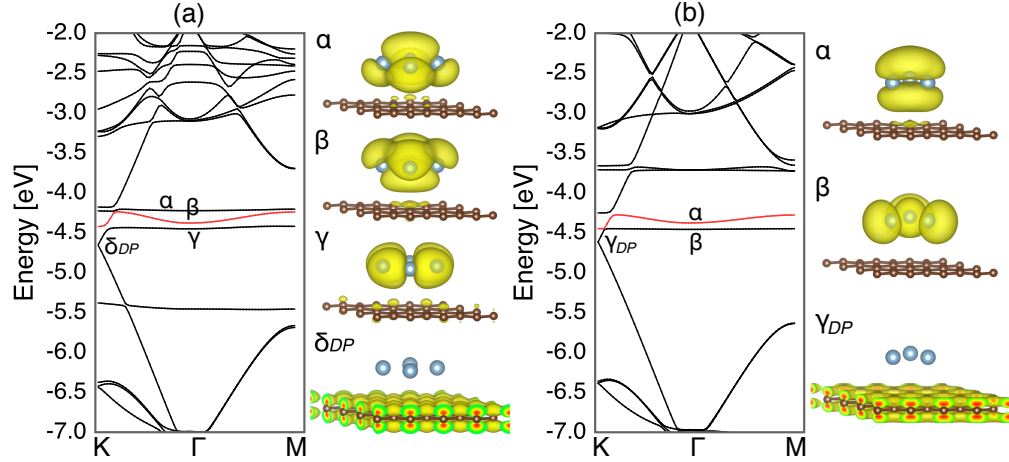


FIGURE 3.2: Electronic energy band of graphene adsorbing (a) Al_4 and (b) Al_3 nanoparticles together with the isosurfaces of the squared wavefunctions at K point labelled in left panels. The red line denotes the partially filled HO state. The energies are measured from that of the vacuum level.

Vanderbilt scheme to describe the interaction between nuclei and electrons [73]. The valence wave functions and charge density were expanded in terms of the plane-wave basis set with cutoff energies of 25 and 225 Ry, respectively. Brillouin zone integration was performed with the Γ -centered $8 \times 8 \times 1$ uniform \mathbf{k} -mesh for self-consistent electronic structure calculations for graphene with 4×4 lateral periodicity, which corresponds to the $32 \times 32 \times 1$ \mathbf{k} -mesh in a primitive 1×1 cell of graphene, resulting in sufficient convergence for the geometric and electronic structures. According to the choice of the \mathbf{k} -mesh, the Brillouin zone integration contains the K and K' points, allowing us to discuss the phenomena associated with the Dirac point. All atoms were fully optimized until the remaining force acting on each atom was less than $0.005 \text{ Ry}/\text{\AA}$ under a fixed lateral lattice constant of 9.83 \AA corresponding to the experimental value of a 4×4 lateral cell of graphene.

3.3 Carrier Distribution and Electronic Properties

Figure 3.2 shows the electronic energy band of graphene adsorbing Al_4 and Al_3 under the zero electric field, respectively. Three and two less dispersive bands emerge just above the Dirac cone for Al_4 and Al_3 , respectively, associated with the electron states of Al nanoparticles. The wave function analysis indicates that these states possess the highest occupied state (HO) of an isolated Al nanoparticle with bonding p states nature. Because the Fermi level is located above the Dirac cone, the electron is transferred from Al nanoparticles to graphene. In accordance with this charge transfer, the Al nanoparticles possess partially filled electron states at the Fermi level and act as charged impurities for carrier injection into graphene. The partially filled flat dispersion bands cause large density of states at the Fermi level and are expected to prevent electrons injection in graphene by the external electric field.

Under the external electric field induced by the gate electrode, injected carriers are

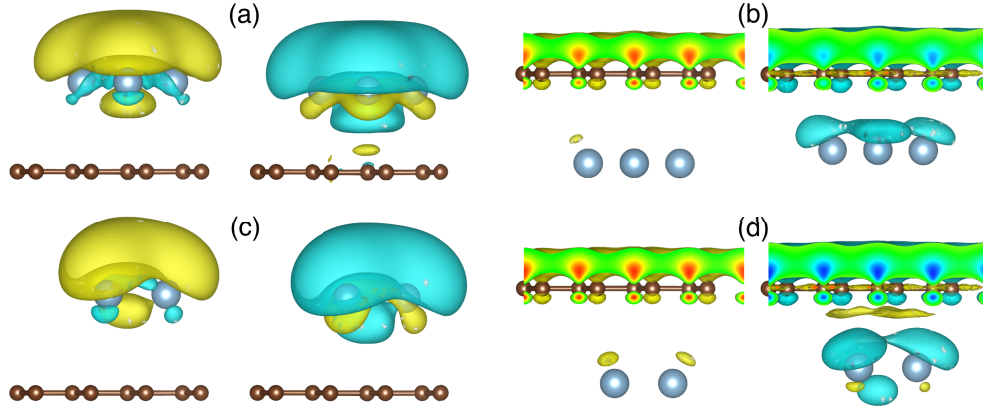


FIGURE 3.3: Isosurfaces of the distribution of the accumulated electrons and holes injected by the gate electrode in graphene- Al_4 hybrids in which Al_4 is adsorbed (a) above and (b) below the graphene layer with respect to the electrode. Isosurfaces of the distribution of the accumulated electrons and holes injected by the gate electrode in graphene- Al_3 hybrids, in which Al_3 is adsorbed (c) above and (d) below the graphene layer. In each figure, the left and right panels show the isosurfaces at $0.3e$ and $0.5h$ doping, respectively. Yellow and blue isosurfaces denote the region where the electrons and holes increase, respectively. Small and large balls denote C and Al atoms, respectively.

mainly accommodated in graphene or Al nanoparticles which are situated at the electrode side [Fig. 3.3]. For the electron doping, the accumulated electrons are primarily distributed on the Al nanoparticles when the Al nanoparticles are sandwiched between graphene and the electrode [Figs. 3.3(a) and 3.3(c)]. The electrons are distributed on the graphene layer when the graphene layer is situated on the electrode side. For the hole injection by the electrode, in the electrode-Al-graphene arrangement, the holes are primarily accommodate into the Al nanoparticles as well as the electron doping. In contrast, when graphene is situated on the electrode side, the accumulated holes exhibit a complex nature. The holes are distributed not only on graphene but also on Al nanoparticles [Figs. 3.3(d) and 3.3(f)]. In addition, the electrons and holes coexist in the spacing between graphene and Al nanoparticle. These facts indicate that the carrier accumulation in graphene is sensitive to the relative arrangement of the metal nanoparticles to the electrode, and metal nanoparticles situated between graphene and electrode may prevent carrier injection into graphene by the electric field.

Figures 3.4 and 3.5 show the electronic energy band of graphene adsorbing Al_4 and Al_3 , respectively, under an external electric field that injects $0.3e$ and $0.5h$ in the hybrid systems. The Dirac point of graphene is insensitive to hole and electron injections for the case when metal nanoparticles are situated between the graphene and metal electrode. In this case, flat dispersion bands associated with metal nanoparticles sensitively shift downward and upward for electron and hole doping, respectively. Therefore, carrier injection into graphene rarely occurs. On the other hand, the Dirac point exhibits downward and upward shifts under electron and hole doping, respectively, for the case when metal nanoparticles are located on the opposite surface of the graphene to the electrode, indicating that carrier injection into graphene is possible under this metal nanoparticle arrangement. Especially, for hole doping the Dirac point approaches the states associated with metal nanoparticles, leading to the orbital hybridization between

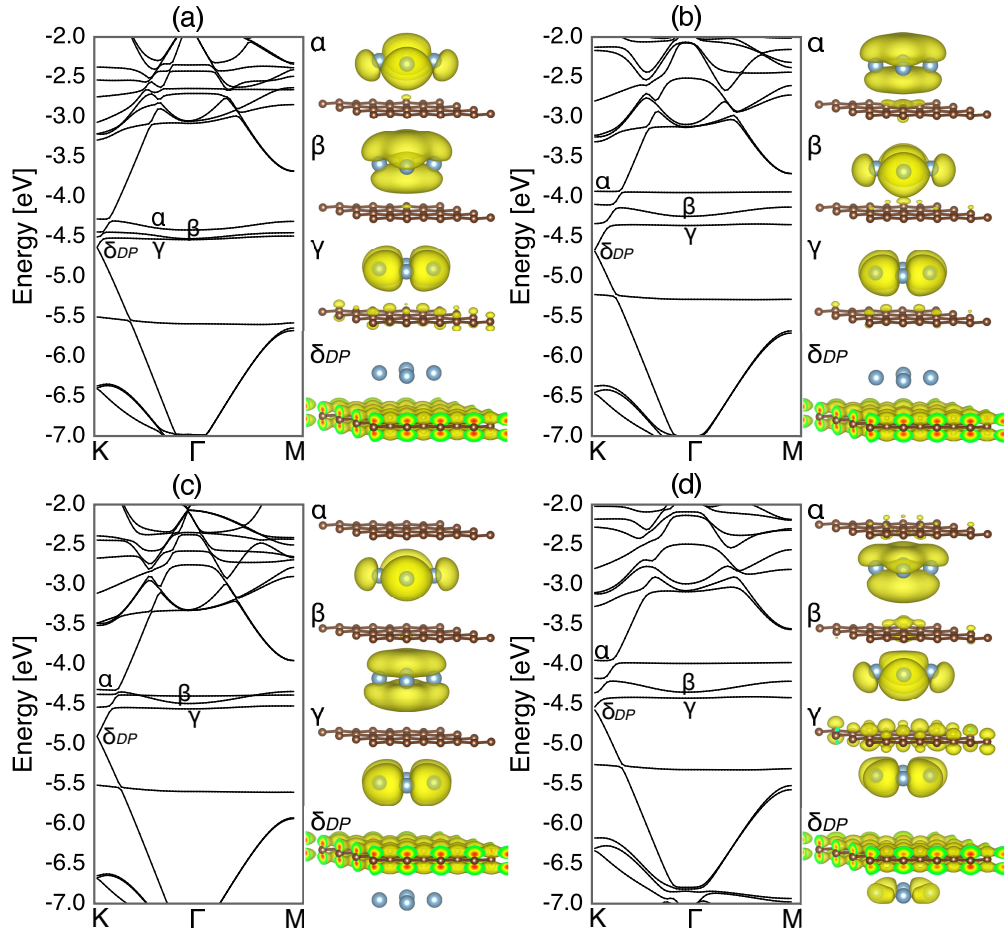


FIGURE 3.4: Electronic energy band of graphene adsorbing Al_4 nanoparticles adsorbed [(a), (b)] above and [(c), (d)] below the graphene layer under equilibrium spacing. The left and right panels show the energy band under 0.3e and 0.5h doping, respectively. The energies are measured from that of the vacuum level. Squared wavefunction at K point near the Fermi level belongs to the electronic states labeled in the band structures on the left side of each wavefunction. The labels α , β , γ indicate the electronic states associated with the Al nanoparticles near the Fermi level. δ_{DP} indicates the electronic state of graphene at the Dirac cone.

the electronic states of graphene and Al nanoparticles. Indeed, the squared wave functions near the Fermi level at the K point show hybridized nature under the hole doping [Figs. 3.4(d) and 3.5(d)]. The orbital hybridization causes the complex carrier distribution in graphene-Al hybrids upon hole doping [Figs. 3.3(b) and 3.3(d)].

Figure 3.6 shows the eigenvalue of the Dirac point and the electronic states associated with Al nanoparticles at the Γ point near the Fermi level as a function of the carrier concentration. The Dirac point (the δ_{DP} and γ_{DP} state) is pinned approximately at an energy of -4.6 eV for the carrier concentrations under the metal arrangement in which metal nanoparticles are situated between graphene and an electrode, indicating that any carriers are rarely injected into graphene by the external electric field [Figs. 3.6(a) and 3.6(c)]. In this case, instead of the almost constant Dirac point, the electron states associated with the metal nanoparticle substantially shift downward with an increasing number of electrons. Injected electrons stabilize the electronic states of metal nanoparticles because the flat band states of Al nanoparticles possess the bonding p state nature

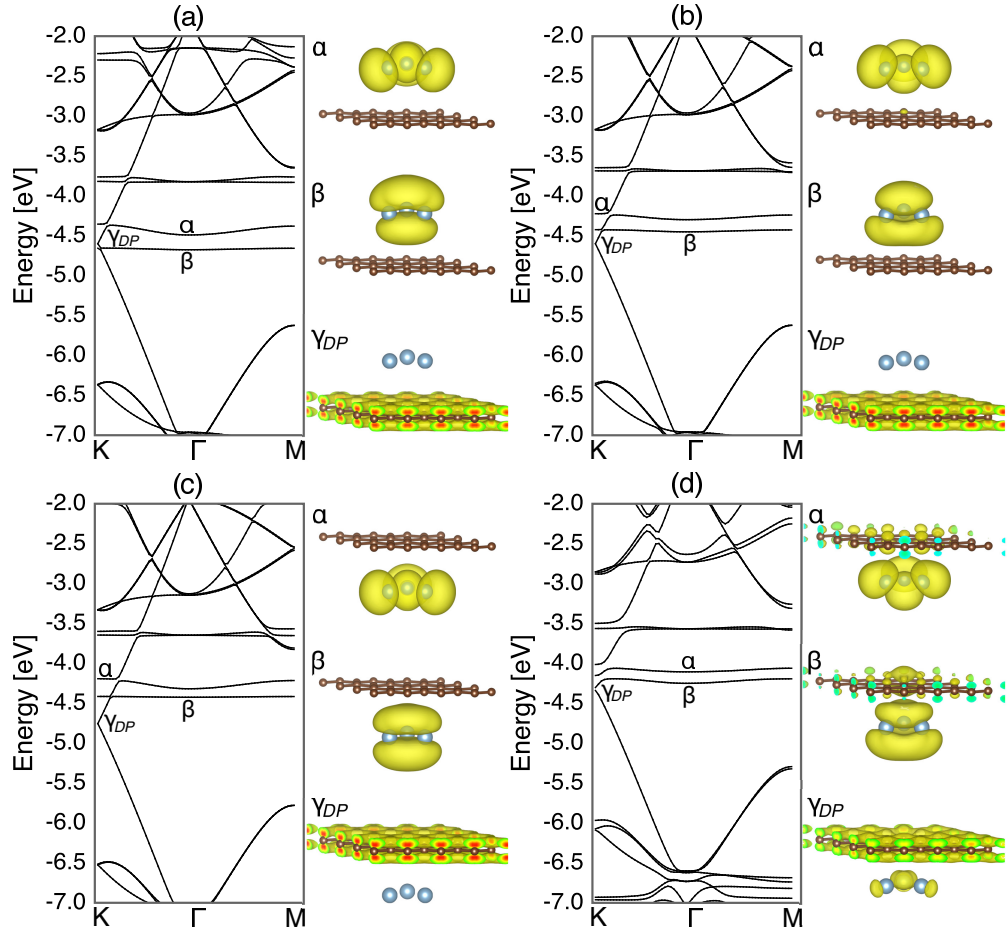


FIGURE 3.5: Electronic energy band of graphene adsorbing Al_3 nanoparticles adsorbed [(a), (b)] above and [(c), (d)] below the graphene layer under equilibrium spacing. The left and right panels show the energy band under $0.3e$ and $0.5h$ doping, respectively. The energies are measured from that of the vacuum level. Squared wavefunction at K point near the Fermi level belongs to the electronic states labeled in the band structures on the left side of each wavefunction. The labels α and β indicate the electronic states associated with the Al nanoparticles near the Fermi level. γ_{DP} indicates the electronic state of graphene at the Dirac cone.

[Fig. 3.2]. In contrast, when the Al nanoparticles are adsorbed on the graphene opposite to the electrode, the carriers are accumulated on the graphene, which causes the downward or upward shift of the Dirac point upon electron or hole doping, respectively, while the electronic states associated with the Al nanoparticles are insensitive to the electron doping [Figs. 3.6(b) and 3.6(d)]. However, for the hole doping, the electronic states of Al nanoparticles simultaneously shift upward following the upward shift of the Dirac point. According to the upward shift of the electronic states of the Al nanoparticles, the holes are injected not only in graphene but also in the Al nanoparticles. The substantial upward shift of the electron states associated with Al nanoparticles is ascribed to the hybridization of wave functions between the Al nanoparticle and graphene under the small equilibrium spacing. It should be noted that the electric field is mostly screened by the Al or graphene situated at the electrode side [Fig. 3.7], although Al nanoparticles and graphene have nanometer size and atomic thickness, respectively. These facts provide guiding principles for designing and controlling physical properties of graphene-based

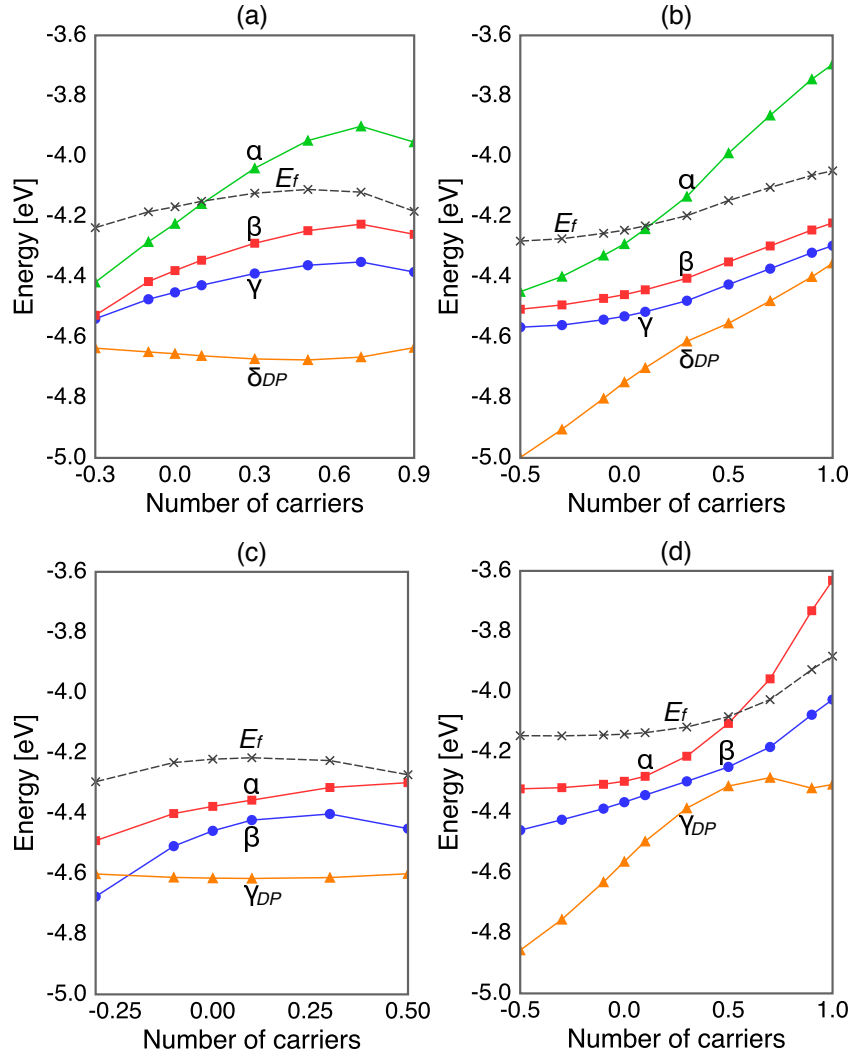


FIGURE 3.6: Energy values of the Dirac point and the electronic states associated with Al nanoparticle at Γ point near the Fermi level as a function of carrier concentration with (a) electrode- Al_4 -graphene, (b) electrode-graphene- Al_4 , (c) electrode- Al_3 -graphene, and (d) electrode-graphene- Al_3 arrangements. The labels in each panel correspond to the electronic states shown in Fig. 3.4 and Fig. 3.5.

FET. To control the Fermi level of the graphene FET, it is necessary to exclude charged nanoparticles from the space between the graphene and electrode.

3.4 Energetics and Geometric Structures

To investigate the stable distance between graphene and the Al nanoparticles, we analyze the total energy of the Al nanoparticles adsorbed on graphene at each carrier concentration as a function of the spacing between them [Fig. 3.8]. The total energy, E , is calculated as

$$E = E_{\text{Gra/Al}}^{\text{F}} - E_{\text{Gra}}^0 - E_{\text{Al}}^0,$$

where $E_{\text{Gra/Al}}^{\text{F}}$, E_{Gra}^0 , and E_{Al}^0 are the total energies of graphene adsorbing Al nanoparticles under the electric field, an isolated graphene without the external field, and an

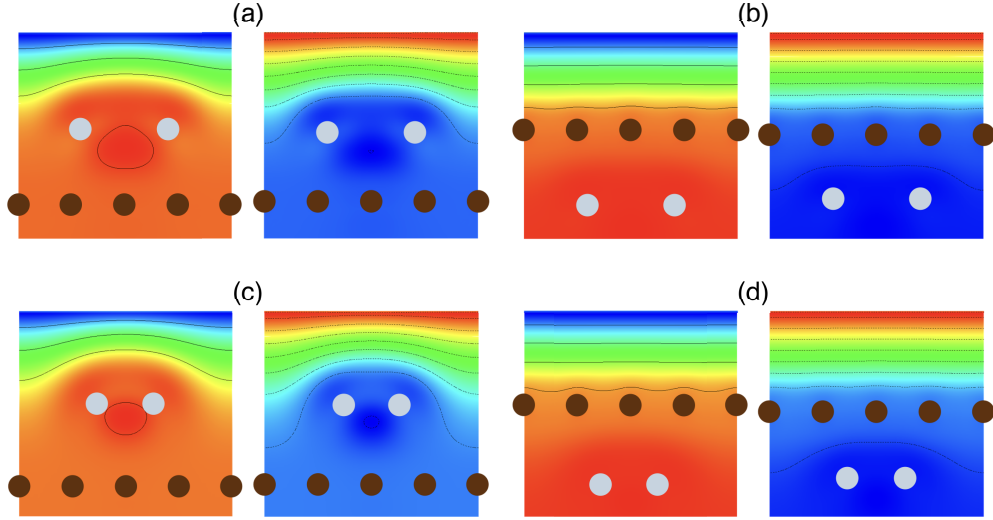


FIGURE 3.7: Contour plots of the electrostatic potential upon electron and hole injections in graphene- Al_4 hybrids in which Al_4 is adsorbed (a) above and (b) below the graphene layer with respect to the electrode. Contour plots of the electrostatic potential upon electron and hole injections in graphene- Al_3 hybrids in which Al_3 is adsorbed (c) above and (d) below the graphene layer with respect to the electrode. In each figure, the left and right panels show the contour plots under $0.3e$ and $0.5h$ doping, respectively. Brown and pale circles denote C and Al atoms, respectively. The counter electrode is located at the top of each panel. Red and blue denote the area corresponding to the high and low electrostatic potentials, respectively.

isolated Al nanoparticle without the field, respectively. The energy minima under the electron/hole doping are shallower than those under the neutral condition except for hole doping when the Al nanoparticles are adsorbed on the surface of graphene opposite to the electrode. This observation indicates that the carrier injection in the hybrids comprising graphene and the Al nanoparticles basically decreases the binding energy of the Al nanoparticles to graphene.

For electron doping, the energy minimum vanishes at the electron concentration of $0.5e/\text{cell}$, indicating that the electron injection desorbs the Al nanoparticles from graphene. The disappearance of the energy minimum under electron doping is ascribed to the Coulomb's interaction arising from the additional electrons injected by the counter electrode. An attractive Coulomb's interaction between negatively charged Al nanoparticles or graphene and the positively charged counter electrode overcomes the binding interaction between the Al nanoparticles and graphene arising from the quantum mechanical effect.

For hole doping, the energy profile is sensitive to the arrangement of the Al nanoparticle relative to the electrode. When the Al nanoparticles are situated on the electrode side, the injected holes induce a strong attractive Coulomb's interaction between the nanoparticles and the negatively charged electrode, resulting in an increase in the spacing between graphene and the Al nanoparticles. On the other hand, the equilibrium spacing monotonically decreases with increasing hole concentration when the Al nanoparticle is located on the surface of graphene opposite to the electrode. Furthermore, the depth of the energy minimum is approximately the same as that under the neutral condition.

As stated above, the equilibrium spacing between graphene and the Al nanoparticles

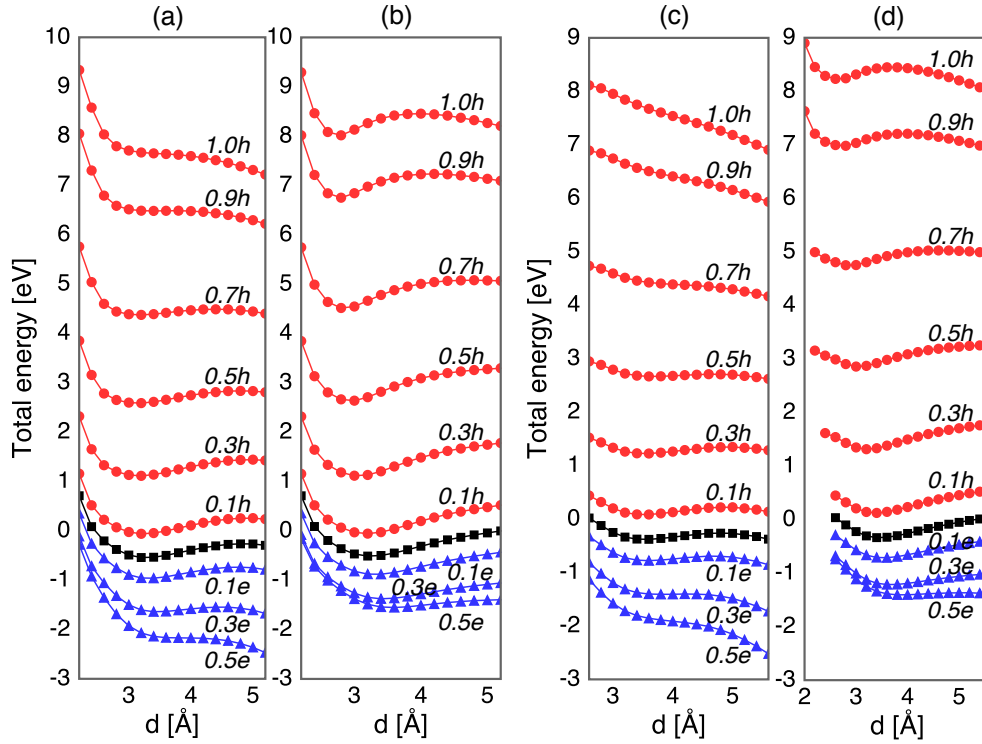


FIGURE 3.8: Total energies of Al_4 adsorbed on graphene with (a) electrode-Al-graphene and (b) electrode-graphene-Al arrangements as a function of spacing between Al_4 and graphene at carrier concentrations from 0.5e to 1.0h. Total energies of Al_3 adsorbed on graphene with (c) electrode-Al-graphene and (d) electrode-graphene-Al arrangements as a function of the spacing between Al_3 and graphene at carrier concentrations from 0.5e to 1.0h. In each panel, filled squares, circles, and triangles denote the total energies under neutral, hole-doped, and electron-doped conditions, respectively.

monotonically increases with increasing the number of electrons, irrespective of the Al nanoparticle arrangement and size [Fig. 3.9]. Furthermore, the Al nanoparticles are desorbed from graphene surfaces at approximately 0.5e doping with the electrode-Al-graphene arrangement, owing to the strong attractive Coulomb's interaction between Al nanoparticles and the counter electrode. For the hole doping, the equilibrium spacing depends on the relative arrangements of the Al nanoparticles with respect to the counter gate electrode. In the case of the Al nanoparticles sandwiched between graphene and the electrode, the equilibrium spacing has minima at the hole concentrations of 0.5h and 0.1h for Al_4 and Al_3 , respectively. Asymmetry of the equilibrium spacing is ascribed to the intrinsic electron transfer from Al nanoparticles to graphene under the zero electric field. Then, the further increase in hole concentration leads to the desorption of the Al nanoparticles at the hole concentrations of 0.9h and 0.5h for Al_4 and Al_3 nanoparticles, respectively, as in the case of the Al nanoparticles under electron doping. In this case, the accumulated holes are localized on the Al nanoparticles, causing a strong attractive interaction with the counter electrode as in the case of electron doping. On the other hand, the equilibrium spacing monotonically decreases with increasing the number of holes when the Al nanoparticles are located at the surface of graphene opposite to the electrode. The equilibrium spacing saturates at approximately 2.6 and 2.4 Å for Al_4 and

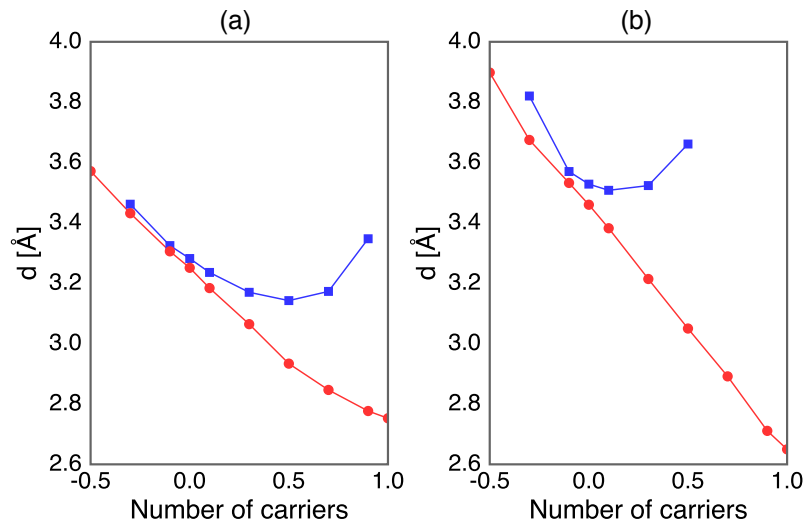


FIGURE 3.9: Equilibrium spacing between Al nanoparticles and graphene as a function of carrier concentration for (a) Al_4 and (b) Al_3 nanoparticles. In each panel, the circles and squares denote the spacing for the electrode-graphene-Al and electrode-Al-graphene arrangements, respectively.

Al_3 nanoparticles, respectively. The small equilibrium spacing between the Al nanoparticles and the graphene layer under hole doping is caused by the orbital hybridization between them [Figs. 3.4(d) and 3.5(d)]. Therefore the hole injection in graphene hybrids with nanoparticles or molecules may generate novel complexes in which adsorbed materials are tightly bound to graphene. Furthermore, the electric field may also promote the chemical reactions of the nanoparticles on graphene.

3.5 Summary

We studied the electronic and geometric structures of Al nanoparticles adsorbed on graphene under excess electron or hole injected by a counter electrode using the DFT combined with the ESM method. Our calculations showed that the Al nanoparticles affect carrier injection in graphene with respect to their mutual arrangement to the electrode. The electron and hole injections are prevented by the metal nanoparticles adsorbed on the surface of graphene to the electrode, leading to the constant energy of the Dirac point of graphene. In contrast, for the case that the Al nanoparticles are adsorbed on the opposite surface of graphene to the electrode, the Dirac point monotonically shifts associated with carrier concentration, indicating that the metal nanoparticles do not affect the carrier injection in graphene by the electric field except hole doping. The stable equilibrium spacing between Al nanoparticles and graphene under excess electron/hole is also sensitive to the carrier species, the carrier concentration, and the Al nanoparticles arrangement with respect to the electrode. The electron injection in hybrids increases the equilibrium spacing, irrespective of the Al nanoparticles arrangement relative to the electrode. In contrast, for hole injection, the equilibrium spacing monotonically decreases with increasing the number of holes when the nanoparticles are situated on the vacuum side, while the equilibrium spacing has a minimum under the

hole concentration that depends on the nanoparticle size when the nanoparticle is sandwiched between graphene and the electrode. The present results may give theoretical insights into a possible procedure to control the geometric structure of nanoparticles in graphene-based FET structures.

Chapter 4

Graphene Adsorbing CO₂ and CO Molecules

In this Chapter, we show the energetics and electronic structures of CO and CO₂ molecules adsorbed on graphene surfaces in the FET structure with respect to the excess electrons/holes by the external electric field.

4.1 Introduction

Graphene is a potential material for functional devices, because of its unique structural and electronic properties. The electronic structure of graphene is fragile against the formation of hybrid structures with foreign materials, such as insulating substrates [83–86], metal electrodes [87], molecular/atomic adsorbates [23, 30, 31, 33, 88, 89, 95, 96], and structural defects [48, 97–99]. Furthermore, an external electric field can tune the electronic structure of graphene and its hybrids [47]. In the previous Chapter, we have explained that metal nanoparticles adsorbed on graphene with a FET structure affect the carrier injection in graphene. Despite the electronic structure of graphene hybrids having been well studied to date, a little is known about the structural properties of graphene hybrids under external perturbations, such as the external electric field and mechanical deformations. These studies may advance the application of graphene in various functional devices, because adsorption phenomena depends on charge density distributions on graphene and adsorbates. Indeed, mechanical strain causes both increases and decreases in the interaction between graphene and adsorbed C₆₀ [100]. Furthermore, optimum adsorbed structures of metal nanoparticles on graphene strongly depend on the carrier density injected by the gate electrode and on their mutual arrangement with respect to the gate electrode associated with the interplay between the electron states of the metal nanoparticles and the small density of states near the Fermi level of graphene [101, 102]. On the other hand, the energetics and geometries of environmental molecules, such as CO_x and NO_x, under the external electric field is still unclear, even though the binding energy and the stable molecular arrangement of such

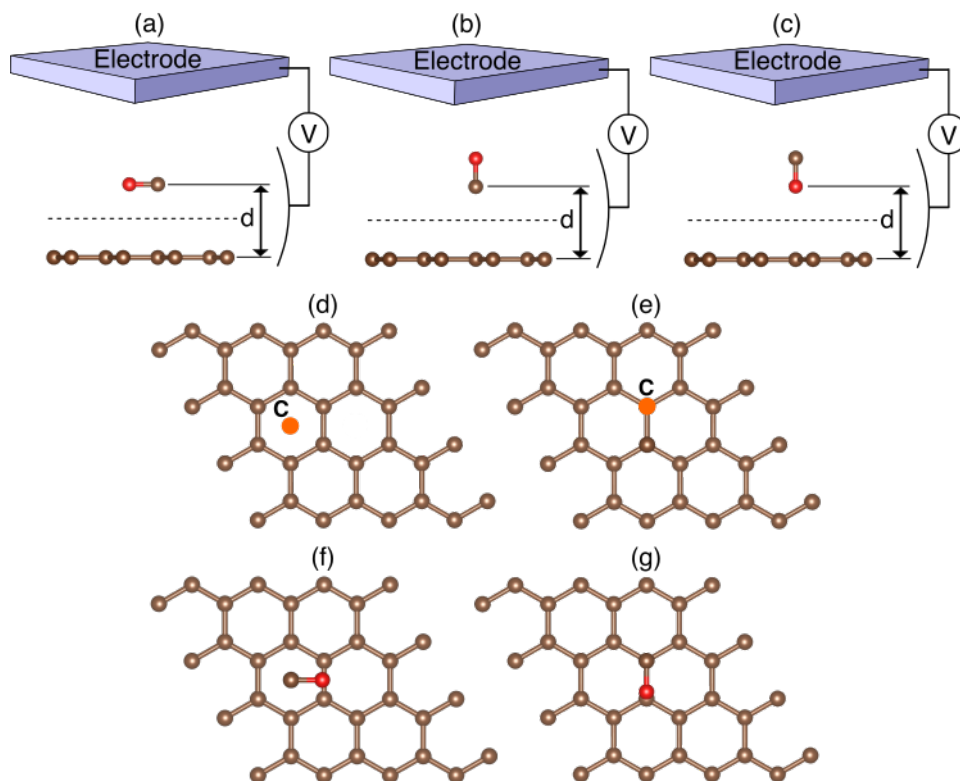


FIGURE 4.1: Structural models of graphene FET adsorbing CO with (a) the lying molecular conformation and the standing molecular conformation where C atom is situated on (b) the graphene and (c) the electrode sides. Top views of the standing molecular conformation adsorbing on (d) hollow and (e) on-top sites and those of the lying molecular conformations adsorbed on (f) hollow and (g) on-top sites of graphene. Red and brown balls denote O and C atoms, respectively. The blue slab above the molecule adsorbed on graphene represents the counter metal electrodes simulated by the ESM.

molecules on graphene are expected to depend on the carrier density and species injected by the gate voltage in FET structures. By analogy with metal nanoparticles on graphene in FET structures, this expectation would certainly further improve or tune the molecular sensing efficiency of graphene-based functional devices.

In this Chapter, using DFT combined with the ESM method, we show the energetics and the geometries of the CO and CO_2 molecules adsorbed on graphene with regard to carrier concentrations and species injected by gate voltage for providing guiding principle to tune and control the binding properties of these molecules to graphene using an electric field.

4.2 Computational Parameters and Structural Models

All calculations on CO and CO_2 adsorbed on graphene were performed based on the DFT [49, 50]. For the calculation of the exchange-correlation energy amongst the interacting electrons, the GGA was used with the Perdew–Burke–Ernzerhof functional form [59]. To describe the weak dispersive interaction between CO_x molecules and graphene,

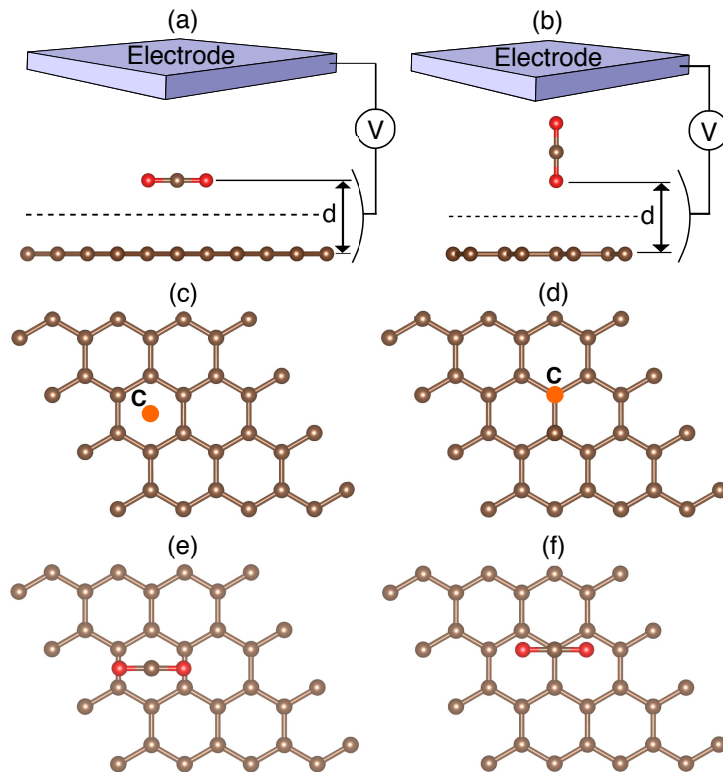


FIGURE 4.2: Structural models of graphene FET adsorbing CO_2 with (a) the lying molecular and (b) the standing molecular conformations. Top views of the standing molecular conformation adsorbing on (c) hollow and (d) on-top sites and those of the lying molecular conformations adsorbed on (e) hollow and (f) on-top sites of graphene. Red and brown balls denote O and C atoms, respectively. The blue slab above the molecule adsorbed on graphene represents the counter metal electrodes simulated by the ESM.

we considered the vdW correction by treating vdW-DF2 with the C09 exchange-correlation functional [61, 66, 68]. We used USPP [73]. The valence wave functions and deficit charge density were expanded in terms of the plane-wave basis set with cutoff energies of 25 and 225 Ry, respectively. Brillouin zone integration was performed with the Γ -centered $8 \times 8 \times 1$ uniform \mathbf{k} -mesh for self-consistent electronic structure calculations for graphene with a 4×4 lateral periodicity, which corresponds to a $32 \times 32 \times 1$ \mathbf{k} -mesh in a primitive 1×1 cell of graphene, resulting in sufficient convergence in the geometric and electronic structures of graphene and its derivatives. With this choice of the \mathbf{k} -mesh, the Brillouin zone integration contains the K and K' points, enabling the phenomena associated with the Dirac point to be analyzed. The geometric structures of CO and CO_2 adsorbed on graphene were fully optimized until the remaining force acting on each atom was less than $0.005 \text{ Ry}/\text{\AA}$ without an electric field. For calculations with an electric field, the internal atomic coordinates of CO and CO_2 adsorbed on graphene are set to those without the electric field.

The ESM method was adopted to investigate the energetics and geometries of graphene adsorbing CO and CO_2 molecules under an external electric field [75]. To inject electrons and holes into CO and CO_2 adsorbed on graphene, we considered a FET structure in

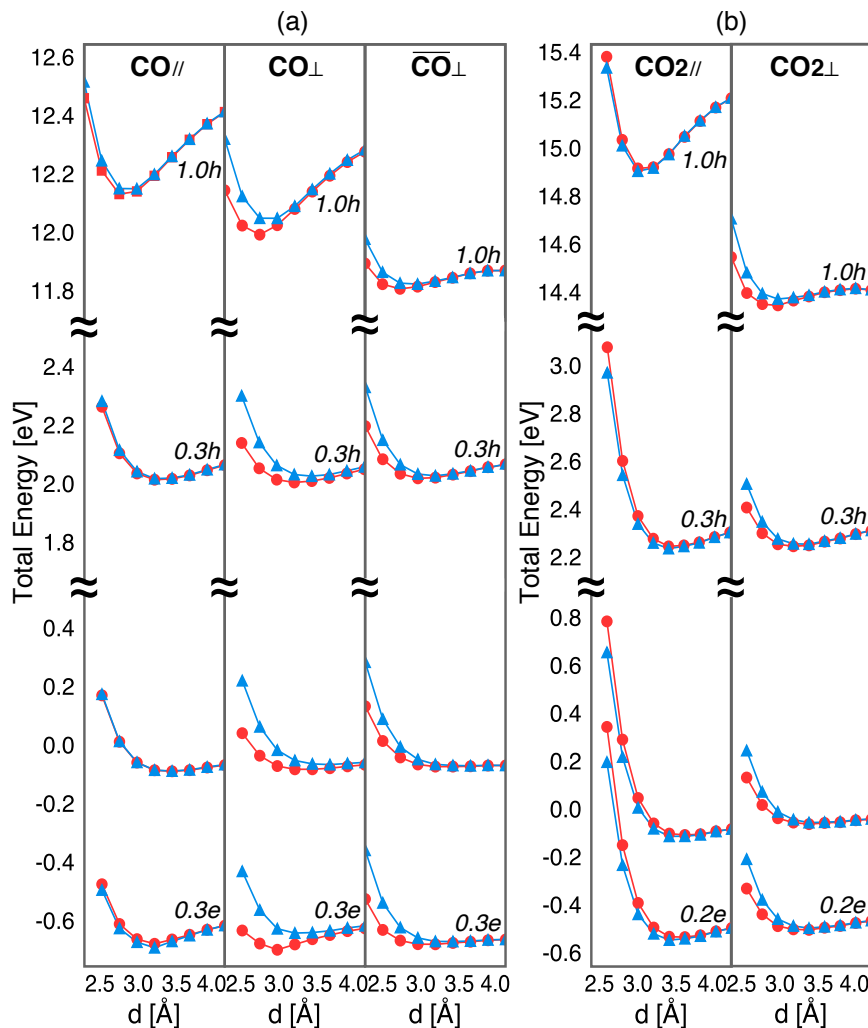


FIGURE 4.3: Total energies of (a) CO and (b) CO_2 adsorbed on graphene as a function of the spacing between adsorbed molecules and graphene under various carrier concentrations. Circles and triangles correspond to the total energy of the C atom in the molecules adsorbed in the hollow sites and on-top sites of graphene, respectively. In each panel, the subscript symbols, $//$ and \perp , indicate the lying and standing molecular conformations, respectively, to graphene. For the CO molecule, center and right panels correspond to the standing conformations in which the C atoms are situated on the graphene and electrode sides, respectively.

which a planar counter electrode described by the ESM with an infinite relative permittivity is situated above the graphene with vacuum spacing of 6.35 and 9.00 Å from the center of mass of the graphene adsorbing CO and CO_2 , respectively [Figs. 4.1 and 4.2]. CO and CO_2 molecules are adsorbed on the electrode side of the graphene surfaces per 4×4 lateral periodicity with two representative molecular conformations characterized by their orientations and positions with regard to the graphene layer.

4.3 Energetics and Geometric Structures Under an External Electric Field

We investigated the total energy of CO and CO₂ adsorbed on graphene with regard to the carrier concentration ranging from 0.3e for CO and 0.2e for CO₂ to 1.0h as a function of their spacing [Fig. 4.3]. The total energy, E , is calculated using

$$E = E_{\text{Gra}/\text{CO}_x}^{\text{F}} - E_{\text{Gra}}^0 - E_{\text{CO}_x}^0,$$

where $E_{\text{Gra}/\text{CO}_x}^{\text{F}}$, E_{Gra}^0 , and $E_{\text{CO}_x}^0$ are the total energies of the graphene adsorbing CO_{*x*} under an electric field, an isolated graphene without the external field, and an isolated CO_{*x*} without the external field, respectively. The energy minima without the electric field are shallow regardless of the molecular species, orientation, and mutual position, indicating that CO_{*x*} is weakly bound to graphene. The calculated binding energy of CO and CO₂ are about 0.1 eV, slightly depending on the molecular species and orientation, which is comparable to the binding energy of them on other two-dimensional materials [103, 104]. For the lying molecular arrangement with regard to the graphene layer, the adsorption property is insensitive to whether they are located in on-top or hollow sites of the graphene network. For a standing molecular arrangement to graphene, the adsorption depends on the mutual orientation and position of molecules with respect to the hexagonal covalent network of graphene. In contrast, by injecting carriers, energy landscapes are substantially modulated, depending on carrier species and concentrations: the energy minima are deepened and the optimum spacing decreases with increasing carrier concentration, except for the standing conformation in which the C atom is located on the electrode side. In particular, molecules in a lying conformation are tightly bound under the injection of carriers compared with conditions encountered without the electric field.

Figure 4.4(a) shows the optimized equilibrium spacing between CO molecule and graphene as a function of carrier concentrations, which is obtained from Fig. 4.3. The equilibrium spacing ranges from about 3.4 to 3.6 Å without the electric field, depending on the mutual molecular position and orientation with respect to the graphene network. For the lying molecular conformation, the optimum spacing is insensitive to the mutual position of CO on graphene. In contrast, the spacing under the standing molecular conformation is sensitive to the mutual position of the molecule on the hexagonal network of graphene. The optimum spacing for the molecule adsorbed on the hollow site is narrower than that for the on-top atomic site. Furthermore, in the standing conformation, the optimum spacing between CO and graphene also depends on whether the C atom is situated at the electrode side. Among all conformations, a standing conformation at an on-top site where the C atom is not situated at the electrode side leads to the largest spacing between CO and graphene. In contrast, a standing conformation at a hollow site where the C atom is situated on the electrode side leads to the smallest spacing. Under carrier injection, the spacing monotonically decreases with increasing electron and hole concentrations, regardless of their molecular conformations. The optimum spacing is narrower by about 0.6 and 0.3 Å under the hole concentration of 1.0h and the electron

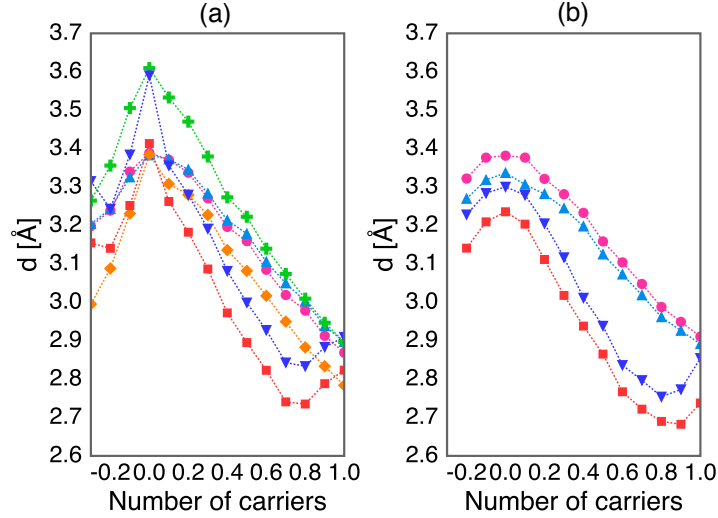


FIGURE 4.4: Equilibrium spacing, d , between adsorbed molecules and graphene as a function of carrier concentration for (a) CO and (b) CO_2 . Circles and triangles correspond to a lying molecular conformation with hollow and on-top adsorption sites, respectively. Squares and inverse triangles (rhombuses and crosses) correspond to a standing molecular conformation with hollow and on-top adsorption sites, respectively, in which for CO molecule the C atom is situated at the electrode side (on the graphene side).

concentration of $0.3e$, respectively. Furthermore, the spacing exhibits an unusual feature for the standing conformation in which the C atom is situated on the electrode side: the spacing again increases with increasing hole concentrations of $0.7h$ or higher and electron concentrations of $0.2e$ or higher.

Figure 4.4(b) shows the optimized equilibrium spacing between CO_2 molecule and graphene as a function of carrier concentrations. With regard to the CO_2 molecule, the spacing is sensitive to the molecular conformation and mutual position with respect to the graphene network. The smallest spacing is about 3.2 \AA under the standing conformation at the hollow site whereas the largest spacing is about 3.4 \AA under the lying conformation at the hollow site without the electric field. Furthermore, the spacing also monotonically decreases with increasing carrier concentration, regardless of their molecular arrangements, except standing conformations under hole concentrations of $0.8h$ or higher.

As stated above, carrier injection deepens the potential landscape of the molecule adsorbed on graphene and decreases its equilibrium spacing. This fact implies that carrier injection can control the binding properties of CO and CO_2 molecules on graphene. To give a quantitative discussion, we analyze the dynamical properties of the adsorbed molecules on graphene by calculating the frequency of molecular oscillations around the equilibrium position on graphene under the various carrier concentrations [Fig. 4.5]. The frequency monotonically increases with increasing numbers of electrons and holes, except for CO and CO_2 in the standing conformation and at high carrier concentration, in which the C atom is situated on the electrode side for CO molecule. The frequencies of CO and CO_2 under the hole concentration of $0.7h$ are higher by about 3 and 2 times, respectively, than those under neutral conditions. Furthermore, the frequency also strongly depends on the molecular conformation for each carrier concentration. For

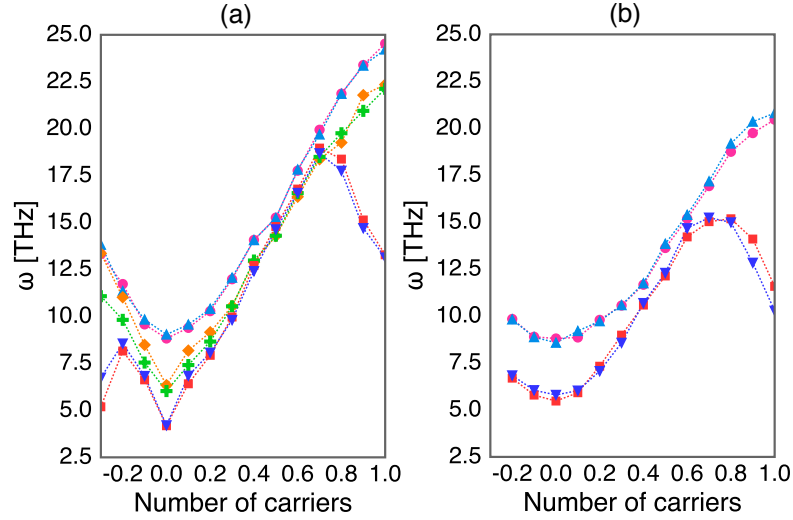


FIGURE 4.5: Frequency of the molecular oscillation of (a) CO and (b) CO_2 molecules around the equilibrium position on graphene as a function of carrier concentration. Circles and triangles correspond to a lying molecular conformation with hollow and on-top adsorption sites, respectively. Squares and inverse triangles (rhombuses and crosses) correspond to a standing molecular conformation with hollow and on-top adsorption sites, respectively, in which for CO molecule the C atom is situated at the electrode side (on the graphene side).

the standing molecular conformation in which the C atom is situated on the electrode side for the CO molecule, the frequency decreases with increasing high carrier concentration; for CO adsorbed on graphene, the electron and hole concentrations are $0.2e$ and $0.7h$ or higher, respectively, and the hole concentration is $0.8h$ or higher in CO_2 adsorption to graphene, in accordance with the increasing equilibrium spacing. Therefore, in THz spectroscopic experiments, we can detect molecular conformations and relative positions with respect to graphene.

Figure 4.6 shows the relative total energy of the CO and CO_2 molecules on graphene with respect to their molecular orientation and position to graphene as a function of carrier concentration. The energies are measured from that of the lying conformation on the hollow and on-top sites for CO and CO_2 , respectively, which corresponds to their ground state molecular arrangements without the electric field. Although the lying conformation is the most stable without the electric field, the injected carriers change their stable molecular orientation from lying to standing. Therefore, CO or CO_2 molecules adsorbed on graphene may undergo a structural phase transition induced by the external electric field. In that case, intermolecular interaction may also affect the molecular conformation on graphene, leading to more complex dependence of their orientation on carrier concentration.

4.4 Carrier Distribution

Figure 4.7 shows the accumulated carrier density injected by the external field for CO and CO_2 adsorbed on graphene under the equilibrium spacing as a function of the z

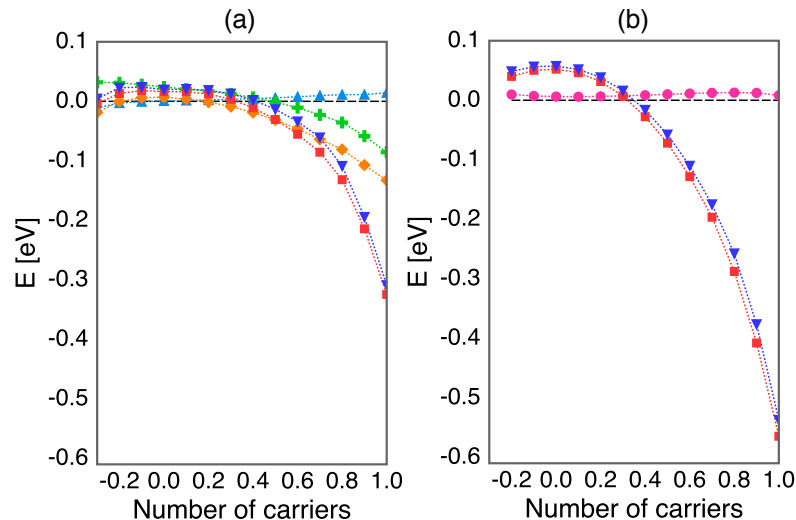


FIGURE 4.6: Relative total energy of (a) CO and (b) CO_2 on graphene as a function of the carrier concentration. The energies are measured from that of the lying molecular arrangement on the hollow and on-top sites for CO and CO_2 , respectively, which correspond to their ground state molecular arrangements without the electric field. Circles and triangles correspond to a lying molecular conformation with hollow and on-top adsorption sites, respectively. Squares and inverse triangles (rhombuses and crosses) correspond to a standing molecular conformation with hollow and on-top adsorption sites, respectively, in which for CO molecule the C atom is situated at the electrode side (on the graphene side).

axis normal to graphene. The distribution of the accumulated carrier depends on the carrier species, molecular species, and their orientation to graphene layer. With electron doping, the electrons are mainly accumulated on the electrode side of the graphene surface. Accordingly, holes and electrons are induced on the graphene and electrode sides of the CO_x molecules, respectively. Thus, the molecules possess a dipole moment with respect to the normal to the graphene surface. With hole doping, similar carrier accumulation occurs. The hole injected into the electrode side of graphene induces electrons and holes on graphene and electrode sides of the molecules, respectively. In this case, a similar dipole moment is induced on the adsorbed molecules by the carrier injection. The Coulomb's interaction between the dipole moment induced on the molecule and the carriers on graphene may enhance the binding energy of these molecule on graphene, leading to the decrease in the equilibrium spacing and the increase in the frequency under hole or electron doping. Furthermore, the distribution of the accumulated carriers on the molecule is sensitive to the molecular orientation. The distribution of the carrier density on the standing molecular conformation is wider than that on the lying one, stabilizing the standing molecular conformation under carrier injection because the Coulomb's interaction between CO_x and graphene is enhanced.

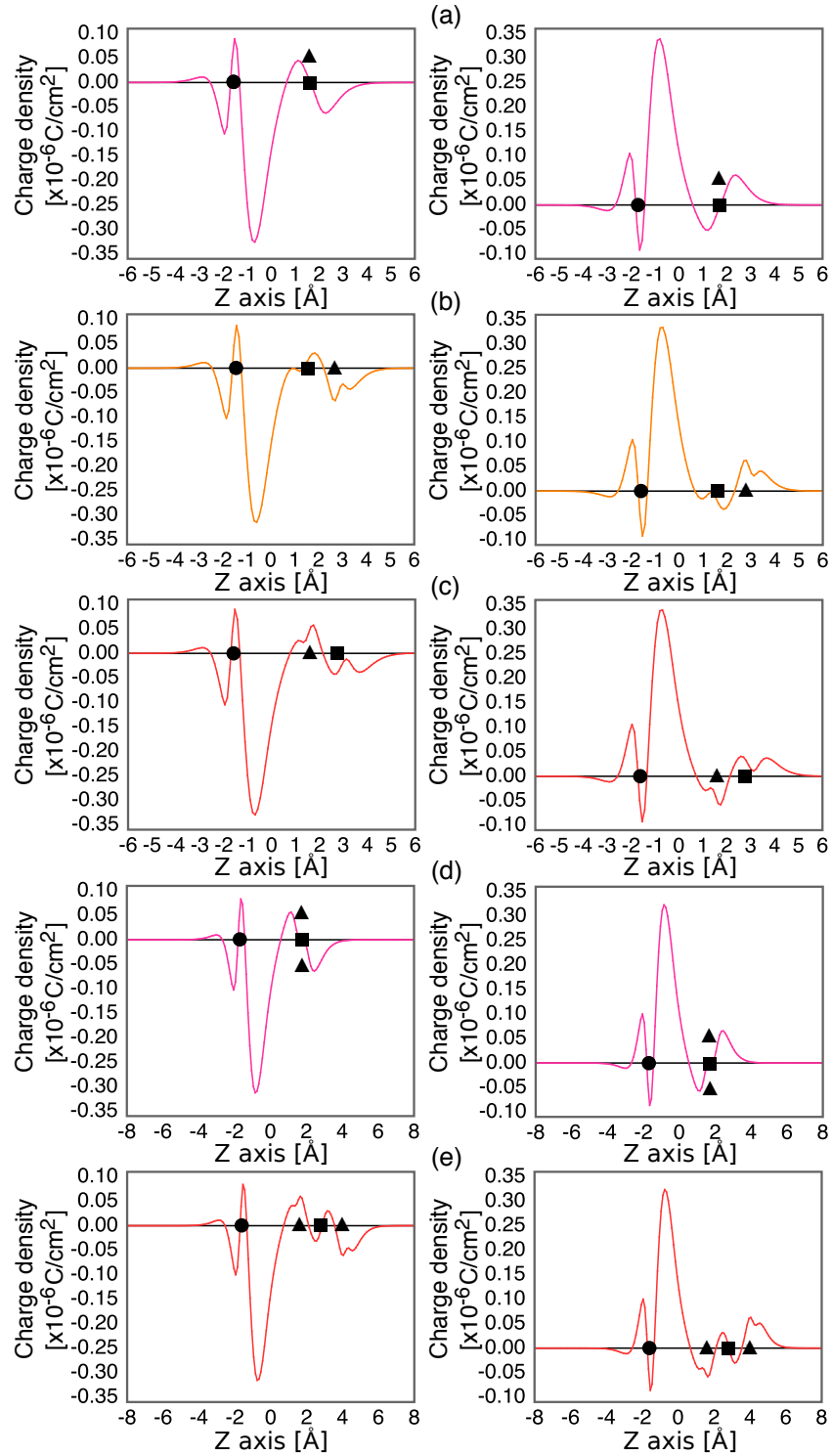


FIGURE 4.7: Plane-integrated charge density of the injected carries in graphene adsorbing CO with (a) the lying conformation and the standing conformations in which the C atom is located on (b) the graphene side and (c) the electrode side. Plane-integrated charge density of the injected carries in graphene adsorbing CO_2 with (d) the lying conformation and (e) the standing conformation. In each figure, the left and right panels correspond with the charge distribution under $0.2e$ and $0.2h$ injection, respectively, by the gate voltage. Circles, squares, and triangles denote positions of the C atoms belonging to graphene, the C atoms belonging to CO_x , and the O atoms, respectively.

The counter electrode is located on the right-hand side of each figure.

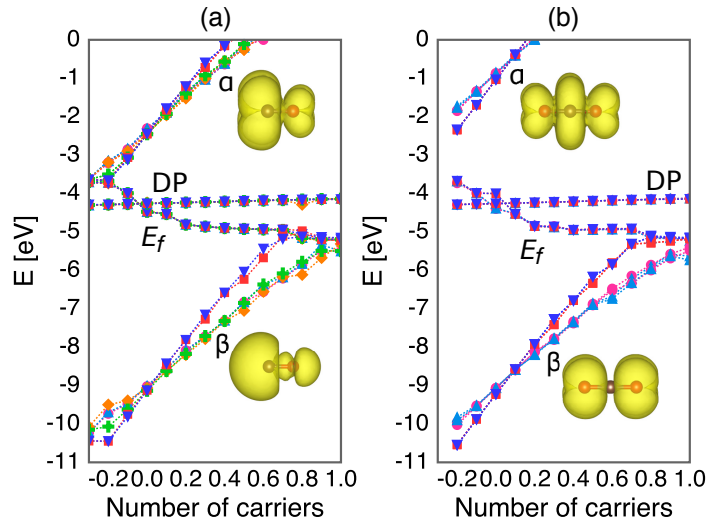


FIGURE 4.8: Electronic structure near the Fermi level of (a) CO and (b) CO_2 adsorbed on graphene as a function of carrier concentration. DP, Fermi level, α , and β indicate the Dirac point of graphene, the Fermi level, the lowest unoccupied states of the adsorbed molecule, and the highest occupied states of the adsorbed molecule, respectively. The insets near α and β indicate the wave functions corresponding to the electronic states of α and β , respectively. Circles and triangles correspond to a lying molecular conformation with hollow and on-top adsorption sites, respectively. Squares and inverse triangles (rhombuses and crosses) correspond to a standing molecular conformation with hollow and on-top adsorption sites, respectively, in which for CO molecule the C atom is situated at the electrode side (on the graphene side).

4.5 Electronic Structures

Figure 4.8 shows the Kohn–Sham states of CO and CO_2 adsorbed on graphene near the Fermi level with respect to carrier concentration. Without the electric field, the electron states associated with the adsorbed molecules are absent near the Fermi level, indicating that the adsorbed molecules do not affect the carrier injection into the graphene under low carrier concentrations. The molecular adsorption to graphene induces modulations of the energy gap between the highest occupied (HO) and the lowest unoccupied (LU) states of CO and CO_2 . The gap is narrower or wider by up to 0.2 eV than that in the isolated forms, depending on molecular species and conformations. The carriers are primarily accommodated within the graphene sheet, leading to a monotonic shift in the Fermi level. The Dirac point retains its energy during carrier injection because of the ridged band nature of electron states of graphene upon the carrier injection. In contrast, the electron states associated with adsorbed molecules vary under carrier injection: eigenvalues of the HO and the LU states of CO and CO_2 molecules monotonically shift downward with increasing electron concentration, whereas they shift upward with increasing hole concentration. For CO adsorption, the HO state of CO in a standing conformation in which the C atom is situated on the electrode side crosses the Fermi level under the hole concentration of 0.7h. The threshold carrier concentration depends on the molecular orientation. For the standing molecular conformation in which the C atom is situated on the electrode side, the threshold carrier concentration is lower than that for other molecular conformations because the distribution of the HO state in

the conformation is closest to the counter electrode among the molecular conformations studied here. Above the critical carrier concentration, the eigenstates associated with CO are insensitive to the carrier injection because the Fermi level is pinned at the HO state of the CO molecule. For CO₂ adsorption, as for CO, the HO state of CO₂ in a standing conformation crosses the Fermi level at the lower hole concentration of 0.8h than that in a lying conformation. Therefore, the adsorbing properties of CO_x molecules on graphene exhibit further variation at high carrier concentrations.

4.6 Summary

Using DFT with the vdW correction and the ESM method, we investigated the energetics, geometries, and electronic properties of CO and CO₂ molecules adsorbed on graphene under the external electric field. Our theoretical investigations found that the binding energies of these molecules on graphene monotonically increased with increasing carrier densities, regardless of the molecular orientation and their relative position to graphene. This fact indicates that the electric field or excess carriers control the binding properties of molecules, thereby enhancing the molecular sensing capability of graphene. Furthermore, detailed analyses regarding the geometric structure clarified that the stable molecular orientation strongly depends on the carrier concentration for both molecules: the lying conformation to graphene is the ground state under neutral conditions, whereas the standing conformation is the ground state under either electron or hole injection, whose critical density is sensitive to the direction of the C atom and the relative position of these molecule on graphene.

Chapter 5

N-doped Graphene

In this Chapter, we show the electronic structure of N-doped graphene under an external electric field to unravel the microscopic mechanisms of the field effect carrier accumulation in N-doped graphene in terms of the defect species, carrier species, and carrier concentration.

5.1 Introduction

N-doped graphene is one of the representative graphene hybrids exhibiting unusual electronic properties that are applicable to electronic and catalytic devices [39, 40, 105–113]. N-doped graphene exhibits rich variation in their local atomic arrangement around N atoms implanted substitutionally in honeycomb network of graphene, because of the different valence of N atoms from that of C atoms: N atoms are incorporated in graphene retaining hexagonal network or forming defects around them [114]. Figure 5.1(a) shows the optimized geometry of the N-doped graphene with the graphitic structure in which the N atom is substitutionally implanted in the graphitic network retaining its hexagonal network. Figure 5.1(b) shows the optimized geometry of N-doped graphene with the pyrrolic structure. For the N-doped graphene with the pyridine structure, we can consider two different structures that contain one and multiple N atoms at the edge of a monatomic vacancy of graphene [Figs. 5.1(c) and 5.1(d)]. It has been reported that the electronic structure of N-doped graphene is sensitive to the local atomic arrangement around N, leading to semiconducting properties with impurity states, which allows them a conducting channel of the transistors. As for the catalytic applications, an experiment showed that the N-doped graphene with pyridinic defects exhibits remarkable catalytic activity for the oxygen reduction reaction compared with those with the other defect species [37, 38, 115, 116]. In such devices, to tailor device properties, it is important to precisely tune the Fermi level. The field effect carrier injection is one of plausible procedure to tune the Fermi level of matters. However, the microscopic mechanism of the Fermi level tuning of the N-doped graphene in terms of the external electric field is still insufficient. Thus, in this Chapter, we show the electronic structure of N-doped

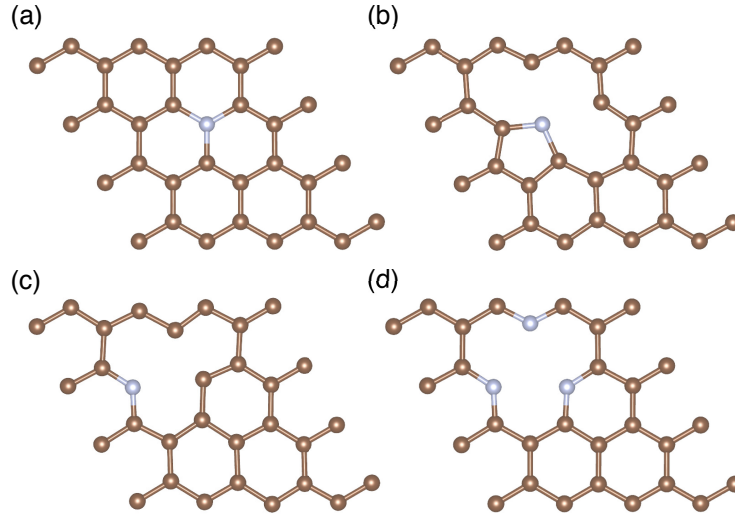


FIGURE 5.1: Optimized geometries of N-doped graphene with (a) graphitic, (b) pyrrolic, (c) pyridinic (pyridinic1), and (d) multiple pyridinic (pyridinic3) structures. The brown and purple circles denote C and N atoms, respectively.

graphene under an external electric field with respect to the arrangements of N atoms in a graphene network, using the DFT combined with the ESM method.

5.2 Computational Parameters and Structural Models

All calculations are conducted using DFT [49, 50] with LDA [58] and USPP [73]. The valence wave functions and deficit charge density were expanded in terms of the plane-wave basis set with cutoff energies of 25 and 225 Ry, respectively. Brillouin-zone integration was performed with the Γ -centered $4 \times 4 \times 1$ uniform \mathbf{k} -mesh for self-consistent electronic structure calculations for N-doped graphene with 4×4 lateral periodicity, which corresponds to the $16 \times 16 \times 1$ \mathbf{k} -mesh in a primitive 1×1 cell of a pristine graphene. All atoms were fully optimized until the remaining force acting on each atom was less than $0.005 \text{ Ry}/\text{\AA}$ under a fixed lateral lattice constant of 9.83 \AA corresponding to the experimental value of a 4×4 lateral cell of graphene.

As for the N-doped graphene, here, we consider four representative structures shown in Fig. 5.1 with 4×4 lateral periodicity. Under the lateral supercell the N and C atoms retain their planar structure after structural optimization. To investigate the electronic properties of N-doped graphene under electron and hole injections, we adopted the ESM method to solve Poisson's equation under a boundary condition in which a planar metal electrode and half-infinite vacuum are situated at two cell boundaries parallel to the graphene layer [75]. Electrons and holes were injected by the planar gate electrode situated at the upper cell boundary with a vacuum spacing of 4.0 \AA to the N-doped graphene layer mimicking the graphene FET with a top gate electrode. The electrode was simulated by the ESM with an infinite relative permittivity. During the calculations under a finite electric field, the atomic structure of the N-doped graphene was fixed as the optimized structure obtained under the zero electric field.

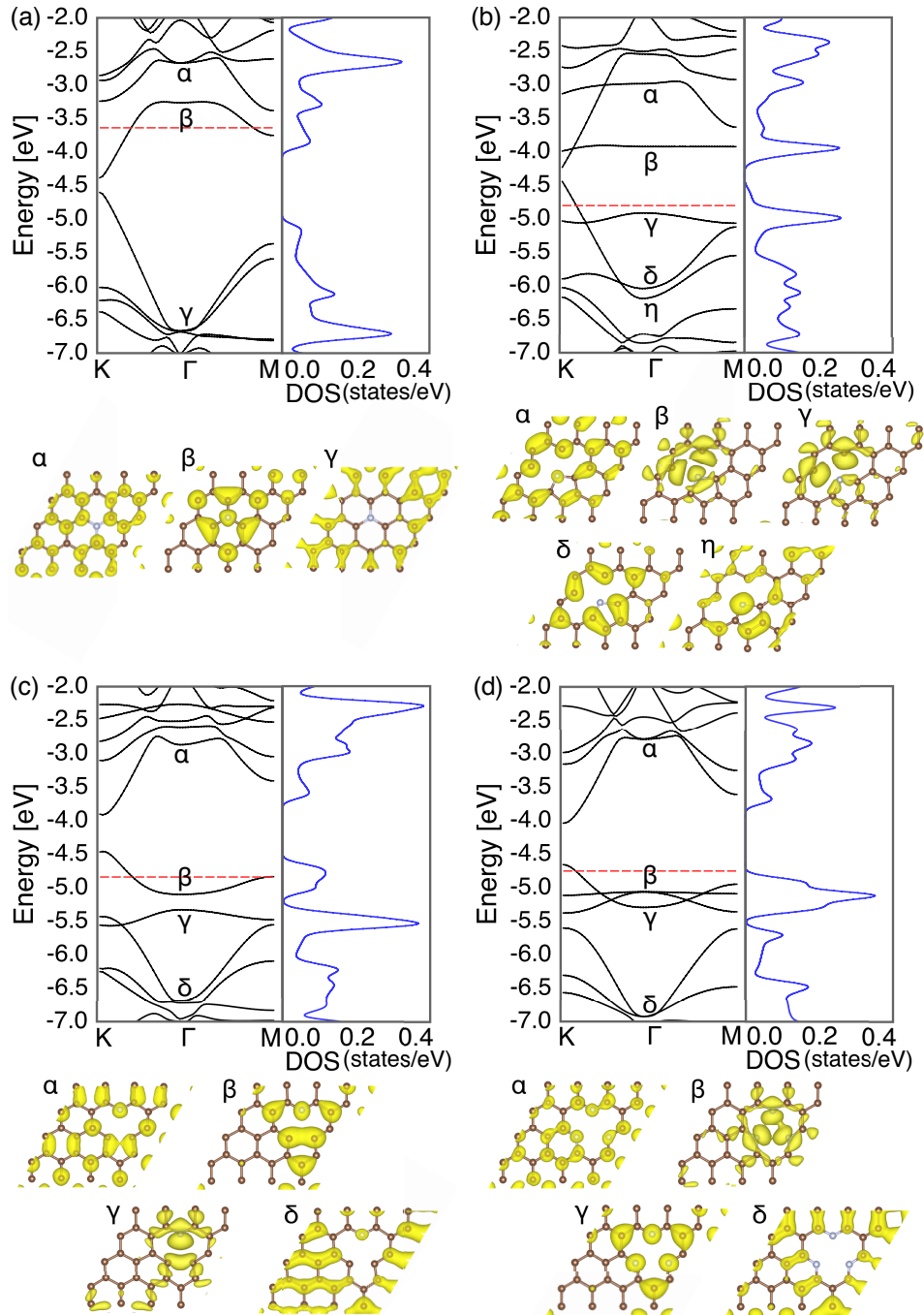


FIGURE 5.2: Electronic structure, density of states, and isosurfaces of squared wave function near the Fermi level of N-doped graphene with (a) graphitic, (b) pyrrolic, (c) pyridinic1, and (d) pyridinic3 structures without the external electric field. Labels assigned to wave function correspond to those in the electronic structure. The horizontal dashed line denotes the Fermi level.

5.3 Electronic Structure

The electronic energy bands of N-doped graphene under a zero electric field are shown in Fig. 5.2. N-doped graphene does not possess the Dirac cone but a finite energy gap in their π electron states irrespective of the defect species. The electronic structures of

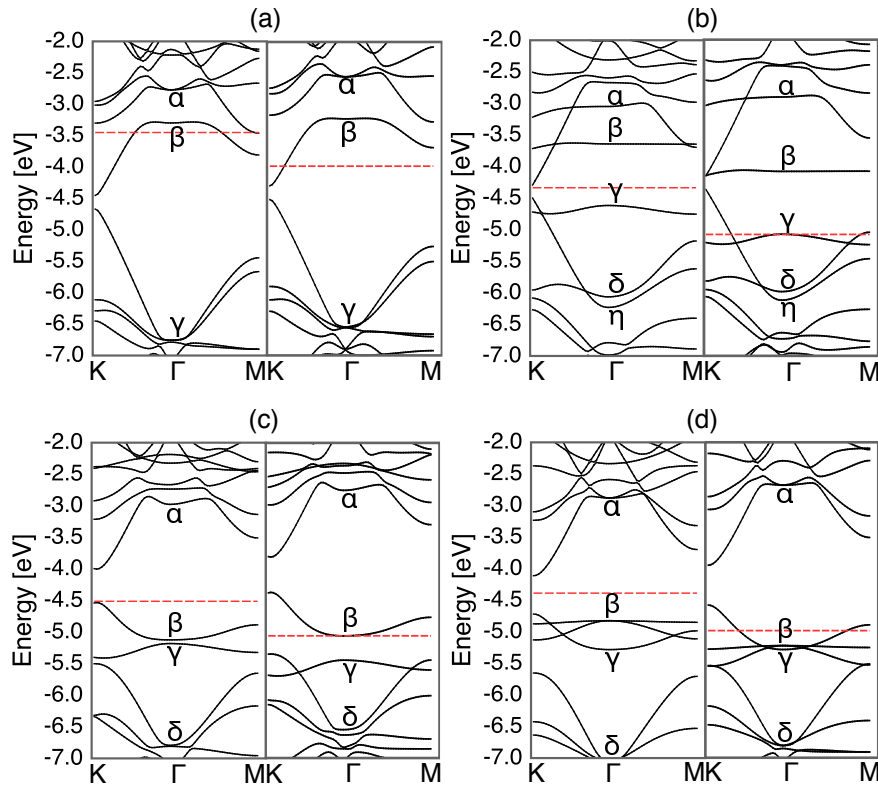


FIGURE 5.3: Electronic structures of N-doped graphene with (a) graphitic, (b) pyrrolic, (c) pyridinic1, and (d) pyridinic3 structures with excess carriers of $0.7e$ and $0.7h$ injected by the counter electrode. In each figure, the left and right panels show the electronic structures under the electron and hole doping, respectively. The red dotted lines denote the Fermi level.

N-doped graphene near the Fermi level are sensitive to the defect species. For graphitic N-doped graphene, the Fermi level crosses the dispersive state labeled β . This state exhibits the nonbonding nature of the π states of graphene localized around the N atomic site together with the antibonding nature of N-C bonds. This state may endow N-doped graphene with a graphitic structure with catalytic activity by the precise tuning of the Fermi level because of its nonbonding nature. For the remaining N-doped graphene structures, pyrrolic and pyridinic graphenes possess two or three less dispersive bands near the Fermi level, which intersect dispersive bands derived from graphene π states. The less dispersive bands are associated with dangling bond states at the defects, e.g., the γ and β states for pyrrolic graphene, the γ state for pyridinic graphene (pyridinic1), and the β state for the other pyridinic graphene (pyridinic3). In addition to the dangling bond states, the nonbonding state forms a less dispersive band near the Fermi level for pyridinic graphene, in which the state also possesses the antibonding nature at the border between N and C atoms.

Figure 5.3 shows the electronic energy band of N-doped graphene under electron and hole doping. The electronic band structure strongly depends on the geometric structure and carrier species. The electronic energy band exhibits the ridged band feature under the electron and hole doping of graphitic N-doped graphene [Fig. 5.3(a)]. In contrast, the electronic structures of the remaining three N-doped graphene structures do not exhibit the ridged band nature. Several less dispersive states shift upward and downward upon

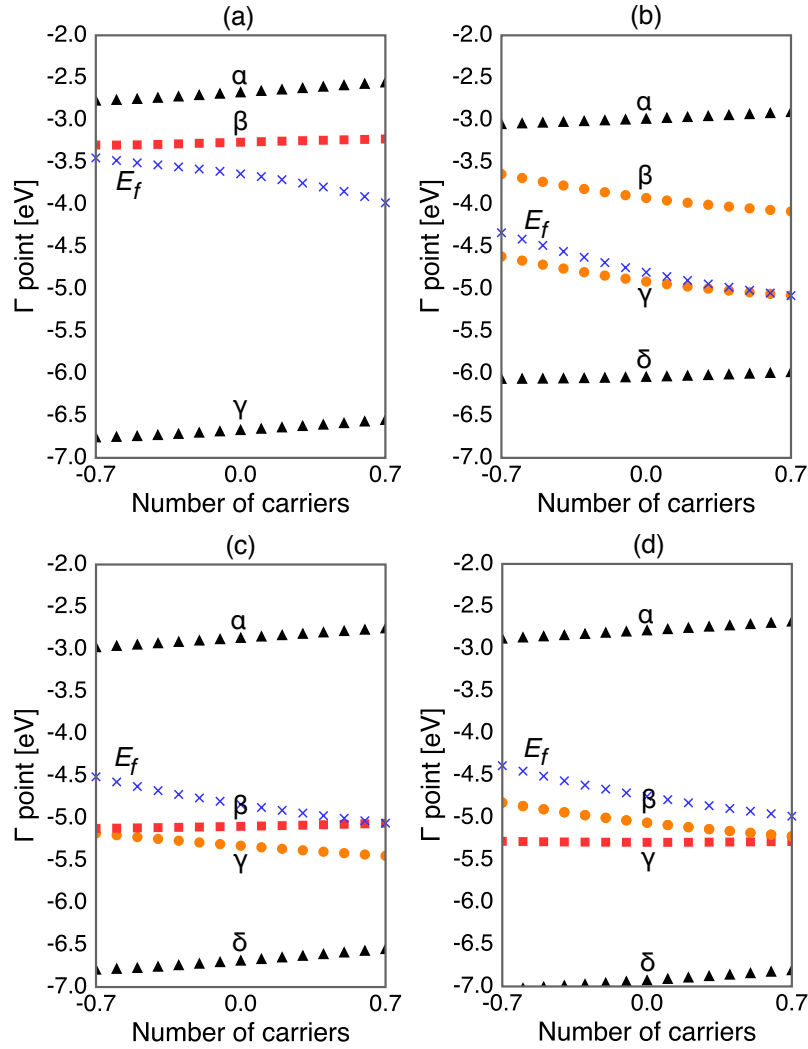


FIGURE 5.4: Fermi level energy and eigenvalues of the electronic states near the Fermi level of N-doped graphene with (a) graphitic, (b) pyrrolic, (c) pyridinic1, and (d) pyridinic3 structures as functions of carrier concentration. Labels correspond to those in the electronic structures in Fig. 5.2. Crosses denote the Fermi level energy.

electron and hole doping, respectively. The two flat band states labelled β and γ exhibit upward and downward shifts caused by the electron and hole injections, respectively, for pyrrolic N-doped graphene [Fig. 5.3(b)]: The γ state is located at the band edge of the dispersive π state by the electron doping, while the β state is located at the band edge of the antibonding π state by the hole doping. The γ and β states are sensitive to the carrier species for the N-doped graphene with the pyridinic1 structure [Fig. 5.3(c)] and the pyridinic3 structure [Fig. 5.3(d)], respectively. These results indicate that the electronic energy band associated with the dangling bond states is sensitive to carrier injection.

To investigate the carrier concentration dependence of the electronic energy band, we investigate the Fermi level energy and the eigenvalue of the electronic states near the Fermi level as functions of carrier concentration [Fig. 5.4]. In all cases, the Fermi level depends on the carrier concentration: The Fermi level shifts upward with increasing

the number of electrons injected in N-doped graphene in contrast to the graphene adsorbing charged impurities, in which the Fermi level is pinned at the energy associated with the eigenstate of the charged nanoparticles [95]. The results indicate that the gate voltage can be used to tune the Fermi level of N-doped graphene regardless of the N arrangements. The eigenvalue at the Γ point associated with the π electron states is insensitive to the carrier concentration for all N-doped graphene structures. In contrast, the eigenvalue at the Γ point associated with the dangling bond state monotonically increases with increasing electron concentration. Therefore, the electron filling of the nonbonding π electron states is tunable by adjusting the external electric field induced by the gate electrode in FET structures. The filling control of these states enhances or deteriorates the chemical reactivity of N-doped graphene under the FET structure. The upward shift of dangling bond states upon electron injection is ascribed to the large onsite Coulomb's repulsive interaction under electron doping in these states. On the other hand, nonbonding π states exhibit a relatively extended nature compared with the dangling bond state, making the states insensitive to electron doping.

The distribution of the accumulated carriers in N-doped graphene under the external electric field is worth investigating. Figure 5.5 shows the isosurfaces of the accumulated carriers in the N-doped graphene with 0.7e and 0.7h under the external electric field. Since the Fermi level crosses the dispersive bands associated with the nonbonding states induced by N doping, injected carriers are primarily accommodated in the nonbonding π states under the finite external electric field. Furthermore, for the N-doped graphene with the pyrrolic and pyridinic structures, the dangling bond states are also located near the Fermi level. Thus, these states also contribute to carrier injection. For the N-doped graphene with the graphitic structure, the injected carriers have the nonbonding π electron nature as the states that cross the Fermi level for both electron and hole doping [Fig. 5.5(a)]. For the N-doped graphene with the pyrrolic and pyridinic structures, the electrons and holes are accommodated in the nonbonding π electron states around the N atoms and the dangling bond states near the Fermi level [Figs. 5.5(b)-5.5(d)]. Because of the upward and downward shifts of the dangling bond states upon electron and hole injections, respectively, these states symmetrically contribute to the carrier injection in N-doped graphene with dangling bond states. Furthermore, the distribution of the accumulated carriers corroborates the physical mechanism that N-doped graphene with the pyrrolic and pyridinic structures does not exhibit the ridged band nature owing to the energy shift of the dangling bond states depending on the carrier concentration.

Figure 5.6 shows the contour plots of electrostatic potential upon the electron and hole injections in N-doped graphene. Because of carrier concentration around the N atom and its adjacent C atoms, the electrostatic potential is spatially modulated within the graphene layer. For the electron doping, the potential near the N atomic site is higher than that near the C atomic site owing to the electron accumulation. On the other hand, the potential around the N atomic site is lower than that around the C atomic site for the hole doping, owing to the electron depression. Since the distribution of accumulated carriers is approximately symmetric for electron and hole doping, the electrostatic potential also exhibits a symmetric feature upon carrier doping. The spatially modulated electrostatic potential implies that carrier injection can control the chemical reactivity of molecules around N atomic sites: molecular adsorptions to N-doped graphene may

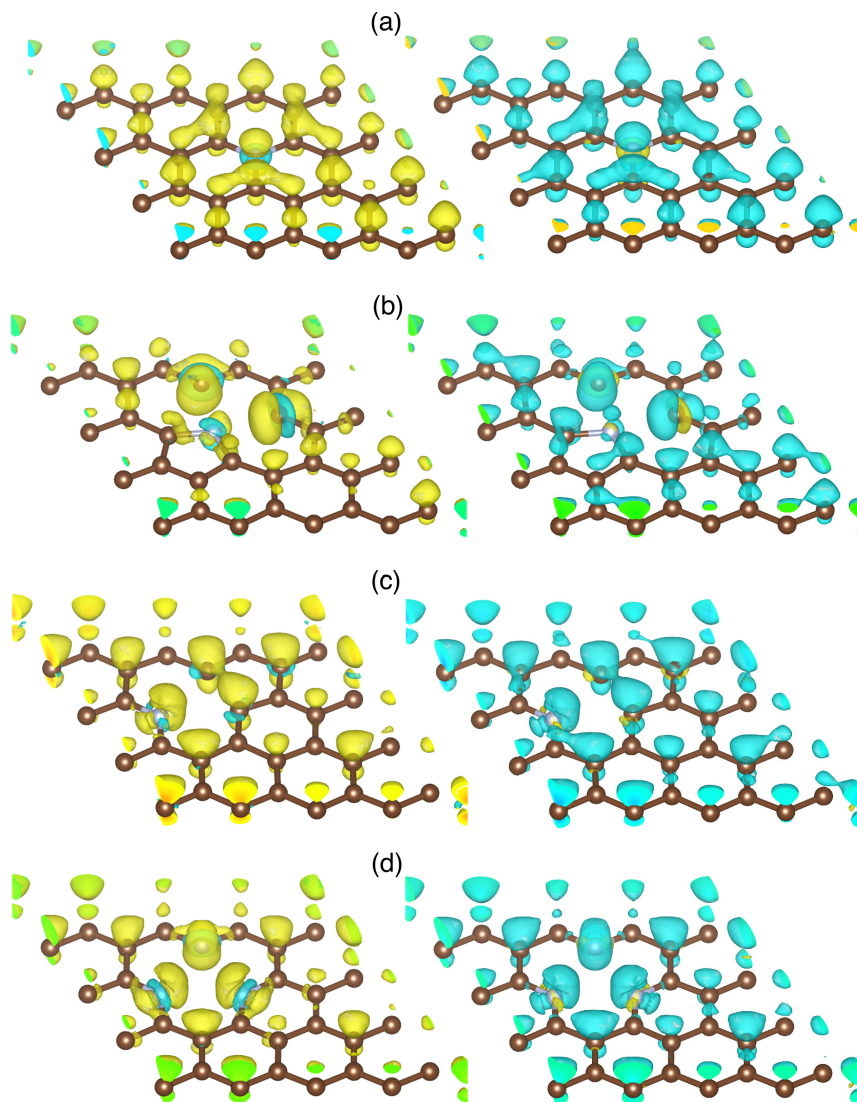


FIGURE 5.5: Isosurfaces of accumulated carrier in N-doped graphene with (a) graphitic, (b) pyrrolic, (c) pyridinic1, and (d) pyridinic3 structures. In each figure, the left and right panels show the isosurfaces under $0.7e$ and $0.7h$ doping, respectively. The yellow and blue surfaces denote the regions of electron accumulation and depression, respectively.

strongly depend on the molecular orientation and carrier concentration, so that the selective adsorption of molecules controls the catalytic reactivity of N-doped graphene in a FET structure.

5.4 Summary

We have studied the electronic structure of N-doped graphene under an external electric field to investigate the possibilities of electron-filling control and the Fermi level tuning of N-doped graphene by the field. Our calculations showed that the electronic states near the Fermi level depend on the carrier concentration injected by the external electric field.

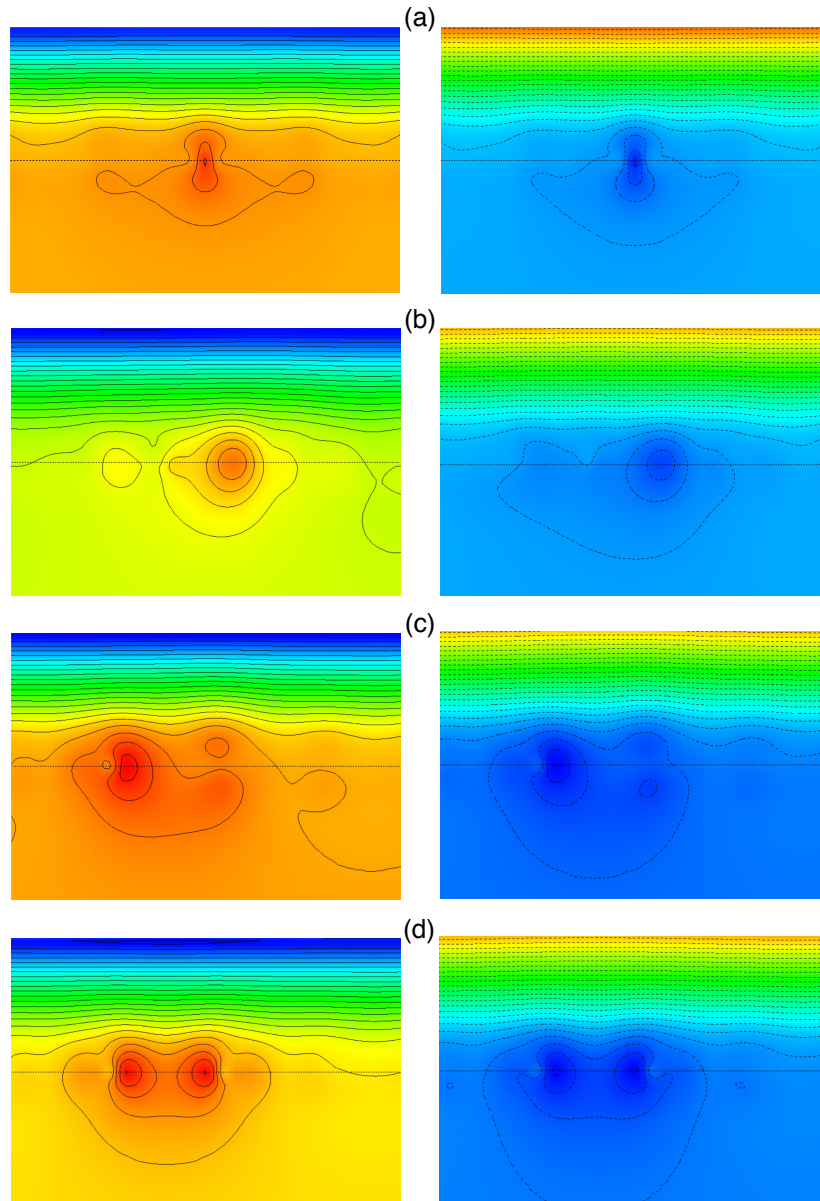


FIGURE 5.6: Contour plots of the electrostatic potential upon electron and hole injections in N-doped graphene with (a) graphitic, (b) pyrrolic, (c) pyridinic1, and (d) pyridinic3 structures. In each figure, the left and right panels show the contour plots under $0.7e$ and $0.7h$ doping, respectively. The vertical dotted lines denote the graphene layer. The counter electrode is located at the top of each panel. Red and blue denote the area corresponding to the high and low electrostatic potentials, respectively. Note that the steep potential variation at the top of each figure corresponds to the electrode region.

The electronic states associated with the dangling bond shift upward and downward with increasing number of electrons and holes, respectively. In contrast, electronic states associated with nonbonding π states almost retain their energy upon carrier injection. We also demonstrated that the Fermi level monotonically shifts upward and downward upon electron and hole injection, respectively. The results indicate that the band filling of the nonbonding π states of N-doped graphene is controllable by adjusting the external electric field. The upward shift of dangling bond states following the Fermi level shift is ascribed to the large Coulomb's repulsive interaction by the injected electron in the states.

Chapter 6

Conclusions

In this thesis, we studied the energetics, geometrics, and electronic properties of graphene derivatives forming hybrid structures with foreign materials under the external electric field, using DFT with ESM method. In particular, we focus on these hybrids in the FET structures in terms of the field-effect carrier injection to provide a fundamental insight into the microscopic mechanism of carrier accumulation in graphene based devices.

In Chapter 3, we studied electronic and geometric properties of graphene physisorbing Al₄ and Al₃ nanoparticles, as representative metal impurities in graphene FET, under an external electric field. Carrier accumulation induced by the gate electric field strongly depends on the nanoparticle position relative to the electrode. When Al nanoparticle is sandwiched between graphene and the electrode, carriers are mainly injected into the Al nanoparticle, preventing carrier injection into graphene. Accordingly, the Dirac point is insensitive to the carrier concentration. In contrast, when the Al nanoparticles are located on the opposite side to the electrode, the carriers are injected into graphene, leading to the Dirac point shift. Furthermore, the stable positions of Al nanoparticles depend on their arrangements to the electrode and on carrier species. When Al nanoparticles are sandwiched between graphene and the electrode, the Al nanoparticles are desorbed from graphene under the high carrier concentration. On the other hand, for the case of the Al nanoparticles adsorbed on the opposite side to the electrode, the optimum spacing monotonically decrease with increasing negative gate voltage, which injects hole, indicating that the binding properties depends on the carrier species and concentrations.

Chapter 4 expressed the energetics, geometries, and electronic properties of graphene adsorbing CO and CO₂ molecules under the external electric field. We demonstrated that the binding energy and stable conformations of adsorbed CO and CO₂ are sensitive to the carrier concentration. Carrier injection decreases the optimum spacing between molecules and graphene, indicating the fact that the injected carrier enhances the molecular binding on graphene because of the Coulomb's interaction between injected carriers in graphene and the induced dipole on the molecules by the external electric field. We further found that the molecular orientation on graphene changes from the lying to standing arrangement by applying the electric field. Thus, the results suggest that the electric field controls the molecular orientation of CO and CO₂ on graphene.

In Chapter 5, we investigated the electronic structure of a N-doped graphene under an external electric field. It is well known that the N-doped graphene possesses various electronic structure depending on the N arrangements in graphene network. The electronic states near the Fermi level are sensitive or insensitive to the carrier injection by the external electric field, depending on their characters. The electron states associated with the dangling bonds shift upward and downward upon electron and hole injections, respectively, because of their localized nature, leading to the large Coulomb's interaction. In contrast, the electron states associated with the nonbonding π states almost retain their eigenvalue upon carrier injection by the external electric field. These facts indicate that the band-filling of the nonbonding π states of N-doped graphene is controllable by adjusting the external electric field.

Appendix A

Hohenberg-Kohn Theorems

Theorem 1: Existence theorem

The external potential $V_{\text{ext}}(\mathbf{r})$ is a unique functional of the ground state electron density $\rho_0(\mathbf{r})$.

Proof of the theorem 1

Assume that a different potential V'_{ext} with the ground state wave function Ψ'_0 derives the same density ρ_0 . Clearly, Ψ'_0 is not identical to Ψ_0 that is the ground state wave function under V_{ext} unless $V'_{\text{ext}} = V_{\text{ext}} + \text{const}$. The ground state wave function Ψ_0 and Ψ'_0 derive the energy eigenvalues of the states E_0 and E'_0 for the Hamiltonian \hat{H} and \hat{H}' , respectively. Since Ψ'_0 is not an eigenstate of \hat{H} together with the minimal property of the ground state energy E_0 , an expectation value of \hat{H} with respect to Ψ'_0 should be higher than E_0 ,

$$\begin{aligned} E_0 < \langle \Psi'_0 | \hat{H} | \Psi'_0 \rangle &= \langle \Psi'_0 | \hat{H}' | \Psi'_0 \rangle + \langle \Psi'_0 | \hat{H} - \hat{H}' | \Psi'_0 \rangle \\ &= E'_0 + \int d\mathbf{r} \rho_0(\mathbf{r}) [V_{\text{ext}}(\mathbf{r}) - V'_{\text{ext}}(\mathbf{r})]. \end{aligned} \quad (\text{A.1})$$

Similarly, we can construct an inequality with respect to \hat{H}' with the energy E'_0 .

$$\begin{aligned} E'_0 < \langle \Psi_0 | \hat{H}' | \Psi_0 \rangle &= \langle \Psi_0 | \hat{H} | \Psi_0 \rangle + \langle \Psi_0 | \hat{H}' - \hat{H} | \Psi_0 \rangle \\ &= E_0 - \int d\mathbf{r} \rho_0(\mathbf{r}) [V_{\text{ext}}(\mathbf{r}) - V'_{\text{ext}}(\mathbf{r})] \end{aligned} \quad (\text{A.2})$$

where the strict inequality is established when the ground state is non-degenerate. Addition of Eq. (A.1) and Eq. (A.2) yields a contradictory inequality: $E_0 + E'_0 < E_0 + E'_0$, leading to a conclusion that the ρ_0 associated with the ground state corresponds with an external potential V_{ext} .

Theorem 2: Variational principle

The exact ground state density $\rho_0(\mathbf{r})$ minimizes the ground state energy $E_0[\rho_0(\mathbf{r})]$.

Proof of the theorem 2

Following the first Hohenberg-Kohn theorem, the ground state electron density ρ_0 uniquely

determines the external potential V_{ext} for the Hamiltonian \hat{H} with the ground state wave function Ψ_0 . Thus, the ground state energy E_0 given by Eq. (2.2) is written as

$$E_0 = \langle \Psi_0 | \hat{H} | \Psi_0 \rangle. \quad (\text{A.3})$$

The different electron density ρ' corresponding to Ψ' leads to

$$E_0 = \langle \Psi_0 | \hat{H} | \Psi_0 \rangle < \langle \Psi' | \hat{H} | \Psi' \rangle \equiv E'. \quad (\text{A.4})$$

Thus, the ground state energy can be obtained by minimizing the total energy with respect to the ρ .

Levy's Constrained Search Formulation

According to the Hohenberg-Kohn theorems, a ground state electron density ρ_0 can be generated from a Hamiltonian with an external potential V_{ext} . Levy and Lieb proposed the constrained search formulation to expand it [117–119]. We first redefine the universal part of the Hohenberg-Kohn energy functional Eq. (2.2):

$$F[\rho] \equiv \min_{\Psi \rightarrow \rho} [\langle \Psi_\rho | \hat{T} + \hat{V}_{ee} | \Psi_\rho \rangle] \quad (\text{A.5})$$

where a constrained minimization is conducted over all many-body wave functions Ψ_ρ with the same density ρ . The functional $F[\rho]$ is obtained for any electron density ρ derived from the N-particle antisymmetric wave functions under following conditions [120]

$$\rho(\mathbf{r}) \geq 0 \quad (\text{A.6})$$

$$\int d\mathbf{r} \rho(\mathbf{r}) = N \quad (\text{A.7})$$

$$\int d\mathbf{r} |\nabla \rho(\mathbf{r})|^{1/2} < \infty. \quad (\text{A.8})$$

Using the $F[\rho]$ with the external potential V_{ext} , the ground state energy E_0 is obtained by minimizing the sum of them with respect to the electron densities.

$$E_0 = \min_{\rho} \left\{ F[\rho] + \int d\mathbf{r} \rho(\mathbf{r}) V_{\text{ext}}(\mathbf{r}) \right\} \quad (\text{A.9})$$

Note that the two step minimization procedure by Levy and Lieb covers degenerate ground states. Therefore the Levy's constrained search can determine the ground state energy with its electron density of any electronic system.

Bibliography

- [1] H. Shi, J. Barker, M. Y. Saïdi, R. Koksang, and L. Morris. Graphite structure and lithium intercalation. *J. Power Sources*, 68:291, 1997.
- [2] K. Sugawara, N. Yamamura, K. Matsuda, W. Norimatsu, M. Kusunoki, T. Sato, and T. Takahashi. Selective fabrication of free-standing ABA and ABC trilayer graphene with/without Dirac-cone energy bands. *NPG Asia Materials*, 10:e466, 2018.
- [3] J.-C. Charlier, X. Gonze, and J.-P. Michenaud. First-principles study of the stacking effect on the electronic properties of graphite(s). *Carbon*, 32:289, 1994.
- [4] K. S. Novoselov, A. K. Geim, S. V. Morozov, D. Jiang, Y. Zhang, S. V. Dubonos, I. V. Grigorieva, and A. A. Firsov. Electric field effect in atomically thin carbon films. *Science*, 306:666, 2004.
- [5] D. G. Papageorgiou, I. A. Kinloch, and R. J. Young. Mechanical properties of graphene and graphene-based nanocomposites. *Prog. Mater. Sci.*, 90:75, 2017.
- [6] C. Lee, X. Wei, J. W. Kysar, and J. Hone. Measurement of the elastic properties and Intrinsic strength of monolayer graphene. *Science*, 321:385, 2008.
- [7] A. A. Balandin, S. Ghosh, W. Bao, I. Calizo, D. Teweldebrhan, F. Miao, and C. N. Lau. Superior thermal conductivity of single-layer graphene. *Nano Lett.*, 8: 902, 2008.
- [8] S. Ghosh, I. Calizo, D. Teweldebrhan, E. P. Pokatilov, D. L. Nika, A. A. Balandin, W. Bao, F. Miao, and C. N. Lau. Extremely high thermal conductivity of graphene: prospects for thermal management applications in nanoelectronic circuits. *Appl. Phys. Lett.*, 92:151911, 2008.
- [9] P. R. Wallace. The band theory of graphite. *Phys. Rev.*, 71:622, 1947.
- [10] A. H. C. Neto, F. Guinea, N. M. R. Peres, K. S. Novoselov, and A. K. Geim. The electronic properties of graphene. *Rev. Mod. Phys.*, 81:109, 2009.
- [11] A. K. Geim and K. S. Novoselov. The rise of graphene. *Nat. Mater.*, 6:183, 2007.
- [12] L. Banszerus, M. Schmitz, S. Engels, J. Dauber, M. Oellers, F. Haupt, K. Watanabe, T. Taniguchi, B. Beschoten, and C. Stampfer. Ultrahigh-mobility graphene devices from chemical vapor deposition on reusable copper. *Sci. Adv.*, 1:e1500222, 2015.

- [13] P. J. Zomer, S. P. Dash, N. Tombros, and B. J. van Wees. A transfer technique for high mobility graphene devices on commercially available hexagonal boron nitride. *Appl. Phys. Lett.*, 99:232104, 2011.
- [14] Y. Zhang, Y. W. Tan, H. L. Stormer, and P. Kim. Experimental observation of the quantum Hall effect and Berry's phase in graphene. *Nature*, 438:201, 2005.
- [15] C. L. Kane and E. J. Mele. Quantum spin hall effect in graphene. *Phys. Rev. Lett.*, 95:226801, 2005.
- [16] L. Brey and H. A. Fertig. Electronic states of graphene nanoribbons studied with the Dirac equation. *Phys. Rev. B*, 73:235411, 2006.
- [17] K. Nakada, M. Fujita, G. Dresselhaus, and M. S. Dresselhaus. Edge state in graphene ribbons: nanometer size effect and edge shape dependence. *Phys. Rev. B*, 54:17954, 1996.
- [18] S. Reich, J. Maultzsch, C. Thomsen, and P. Ordejón. Tight-binding description of graphene. *Phys. Rev. B*, 66:035412, 2002.
- [19] J. W. G. Wilder, L. C. Venema, A. G. Rinzler, R. E. Smalley, and C. Dekker. Electronic structure of atomically resolved carbon nanotubes. *Nature*, 391:59, 1998.
- [20] S. Okada and A. Oshiyama. Nanometer-scale ferromagnet: carbon nanotubes with finite length. *J. Phys. Soc. Jpn.*, 72:1510, 2003.
- [21] E. Bekyarova, M. E. Itkis, P. Ramesh, C. Berger, M. Sprinkle, W. A. de Heer, and R. C. Haddon. Chemical modification of epitaxial graphene: spontaneous grafting of aryl groups. *J. Am. Chem. Soc.*, 131:1336, 2009.
- [22] L. S. Panchakarla, K. S. Subrahmanyam, S. K. Saha, A. Govindaraj, H. R. Krishnamurthy, U. V. Waghmare, and C. N. R. Rao. Synthesis, structure, and properties of boron- and nitrogen-doped graphene. *Adv. Mater.*, 21:4726, 2009.
- [23] M. Igami, S. Okada, and K. Nakada. Electronic and geometric structures of fluorine adsorbed graphene. *Synth. Met.*, 121:1233, 2001.
- [24] F. Withers, M. Dubois, and A. K. Savchenko. Electron properties of fluorinated single-layer graphene transistor. *Phys. Rev. B*, 82:073403, 2010.
- [25] H. Sahin, M. Topsakal, and S. Ciraci. Structures of fluorinated graphene and their signatures. *Phys. Rev. B*, 83:115432, 2011.
- [26] J.-A. Yan, L. Xian, and M. Y. Chou. Structural and electronic properties of oxidized graphene. *Phys. Rev. Lett.*, 103:086802, 2009.
- [27] D. Pandey, R. Reifengerger, and R. Piner. Scanning probe microscopy study of exfoliated oxidized graphene sheets. *Surf. Sci.*, 602:1607, 2008.
- [28] E. Clar. *The aromatic sextet*. John Wiley and Sons Ltd., 1972.

- [29] R. Balog, B. Jørgensen, L. Nilsson, M. Andersen, E. Rienks, M. Bianchi, M. Fanetti, E. Lægsgaard, A. Baraldi, S. Lizzit, Z. Sljivancanin, F. Besenbacher, B. Hammer, T. G. Pedersen, P. Hofmann, and L. Hornekær. Bandgap opening in graphene induced by patterned hydrogen adsorption. *Nat. Mater.*, 9:315, 2010.
- [30] Y.-H. Zhang, Y.-B. Chen, K.-G. Zhou, C.-H. Liu, J. Zeng, H.-L. Zhang, and Y. Peng. Improving gas sensing properties of graphene by introducing dopants and defects: a first-principles study. *Nanotechnology*, 20:185504, 2009.
- [31] T. O. Wehling, K. S. Novoselov, S. V. Morozov, E. E. Vdovin, M. I. Katsnelson, A. K. Geim, and A. I. Lichtenstein. Molecular doping of graphene. *Nano Lett.*, 8:173, 2008.
- [32] S. M. Kozlov, F. Vines, and A. Gorling. Bandgap engineering of graphene by physisorbed adsorbates. *Adv. Mater.*, 2011:2638, 2011.
- [33] F. Schedin, A. K. Geim, S. V. Morozov, E. W. Hill, P. Blake, M. I. Katsnelson, and K. S. Novoselov. Detection of individual gas molecules adsorbed on graphene. *Nat. Mater.*, 6:652, 2007.
- [34] N. Shima and H. Aoki. Electronic structure of super-honeycomb systems: A peculiar realization of semimetal/semiconductor classes and ferromagnetism. *Phys. Rev. Lett.*, 71:4389, 1993.
- [35] O. V. Yazyev and L. Helm. Defect-induced magnetism in graphene. *Phys. Rev. B*, 75:125408, 2007.
- [36] T. G. Pedersen, C. Flindt, J. Pedersen, N. A. Mortensen, A.-P. Jauho, and K. Pedersen. Graphene antidot Lattices: designed defects and spin qubits. *Phys. Rev. Lett.*, 100:136804, 2008.
- [37] D. Geng, Y. Chen, Y. Chen, Y. Li, R. Li, X. Sun, S. Yeb, and S. Knights. High oxygen-reduction activity and durability of nitrogen-doped graphene. *Energy Environ. Sci.*, 4:760, 2011.
- [38] L. Qu, Y. Liu, J.-B. Baek, and L. Dai. Nitrogen-doped graphene as efficient metal-free electrocatalyst for oxygen reduction in fuel cells. *ACS Nano*, 4:1321, 2010.
- [39] Y. Fujimoto and S. Saito. Formation, stabilities, and electronic properties of nitrogen defects in graphene. *Phys. Rev. B*, 84:245446, 2011.
- [40] Y. Fujimoto and S. Saito. Hydrogen adsorption and anomalous electronic properties of nitrogen-doped graphene. *J. Appl. Phys.*, 115:153701, 2014.
- [41] E. McCann. Asymmetry gap in the electronic band structure of bilayer graphene. *Phys Rev. B*, 74:161403, 2006.
- [42] H. Miyazaki, K. Tsukagoshi, A. Kanda, M. Otani, and S. Okada. Influence of disorder on conductance in bilayer graphene under perpendicular electric field. *Nano Lett.*, 10:3888, 2010.

- [43] E. McCann and M. Koshino. The electronic properties of bilayer graphene. *Rep. Prog. Phys.*, 76:056503, 2013.
- [44] J. B. Oostinga, H. B. Heersche, X. Liu, A. F. Morpurgo, and L. M. K. Vandersypen. Gate-induced insulating state in bilayer graphene devices. *Nat. Mater.*, 7:151, 2008.
- [45] H. Min, B. Sahu, S. K. Banerjee, and A. H. MacDonald. Ab initio theory of gate induced gaps in graphene bilayers. *Phys. Rev. B*, 75:155115, 2007.
- [46] Y. Zhang, T.-T. Tang, C. Girit, Z. Hao, M. C. Martin, A. Zettl, M. F. Crommie, Y. R. Shen, and F. Wang. Direct observation of a widely tunable bandgap in bilayer graphene. *Nature*, 459:820, 2009.
- [47] M. Otani and S. Okada. Field-induced free-electron carriers in graphite. *J. Phys. Soc. Jpn.*, 79:073701, 2010.
- [48] K. Kishimoto and S. Okada. Fermi-level pinning of bilayer graphene with defects under an external electric field. *Appl. Phys. Lett.*, 110:011601, 2017.
- [49] P. Hohenberg and W. Kohn. Inhomogeneous electron gas. *Phys. Rev.*, 136:B864, 1964.
- [50] W. Kohn and L. J. Sham. Self-consistent equations including exchange and correlation effects. *Phys. Rev.*, 140:A1133, 1965.
- [51] T. Tsuneda. *Fundamentals of density functional theory*. Kodansha Ltd., 2012.
- [52] M. Martin. *Fundamentals of density functional theory*. Cambridge Univ., 2004.
- [53] R. G. Parr and W. Yang. *Density-functional theory of atoms and molecules*. Oxford Univ., 1994.
- [54] J. P. Perdew and A. Zunger. Self-interaction correction to density-functional approximations for many-electron systems. *Phys. Rev. B*, 23:5048, 1981.
- [55] D. M. Ceperley and B. J. Alder. Ground state of the electron gas by a stochastic method. *Phys. Rev. Lett.*, 45:566, 1980.
- [56] R. O. Jones and O. Gunnarsson. The density functional formalism, its applications and prospects. *Rev. Mod. Phys.*, 61:689, 1989.
- [57] O. Gunnarsson and B. I. Lundqvist. Exchange and correlation in atoms, molecules, and solids by the spin-density-functional formalism. *Phys. Rev. B*, 13:4274, 1976.
- [58] J. P. Perdew and Y. Wang. Accurate and simple analytic representation of the electron-gas correlation energy. *Phys. Rev. B*, 45:13244, 1992.
- [59] J. P. Perdew, K. Burke, and M. Ernzerhof. Generalized gradient approximation made simple. *Phys. Rev. Lett.*, 77:3865, 1996.

- [60] K. Berland, V. R. Cooper, K. Lee, E. Schröder, T. Thonhauser, P. Hyldgaard, and B. I. Lundqvist. van der Waals forces in density functional theory: a review of the vdW-DF method. *Rep. Prog. Phys.*, 78:066501, 2015.
- [61] V. R. Cooper. Van der Waals density functional: an appropriate exchange functional. *Phys. Rev. B*, 81:161104, 2010.
- [62] J. P. Perdew and K. Burke. Comparison shopping for a gradient-corrected density functional. *Int. J. Quant. Chem.*, 57:309, 1996.
- [63] P. S. Svendsen and U. von Barth. Gradient expansion of the exchange energy from second-order density response theory. *Phys. Rev. B*, 54:17402, 1996.
- [64] J. P. Perdew and W. Yue. Accurate and simple density functional for the electronic exchange energy: generalized gradient approximation. *Phys. Rev. B*, 33:8800(R), 1986.
- [65] M. Dion, H. Rydberg, E. Schroder, D. C. Langreth, and B. I. Lundqvist. Van der Waals density functional for general geometries. *Phys. Rev. Lett.*, 92:246401, 2004.
- [66] K. Lee, È. D. Murray, L. Kong, B. I. Lundqvist, and D. C. Langreth. Higher-accuracy van der Waals density functional. *Phys. Rev. B*, 82:081101, 2010.
- [67] Y. Zhang and W. Yang. Comment on "generalized gradient approximation made simple". *Phys. Rev. Lett.*, 80:890, 1998.
- [68] I. Hamada and M. Otani. Comparative van der Waals density-functional study of graphene on metal surfaces. *Phys. Rev. B*, 82:153412, 2010.
- [69] P. A. Christiansen, Y. S. Lee, and K. S. Pitzer. Improved ab initio effective core potentials for molecular calculations. *J. Chem. Phys.*, 71:4445, 1979.
- [70] M. Krauss and W. J. Stevens. Effective potentials in molecular quantum chemistry. *Ann. Rev. Phys. Chem.*, 35:357, 1984.
- [71] D. R. Hamann, M. Schlüter, and C. Chiang. Norm-conserving pseudopotentials. *Phys. Rev. Lett.*, 43:1494, 1979.
- [72] N. Troullier and J. L. Martins. Efficient pseudopotentials for plane-wave calculations. *Phys. Rev. B*, 43:1993, 1991.
- [73] D. Vanderbilt. Soft self-consistent pseudopotentials in a generalized eigenvalue formalism. *Phys. Rev. B*, 41:7892, 1990.
- [74] K. Laasonen, A. Pasquarello, R. Car, C. Lee, and D. Vanderbilt. Car-Parrinello molecular dynamics with Vanderbilt ultrasoft pseudopotentials. *Phys. Rev. B*, 47:10142, 1993.
- [75] M. Otani and O. Sugino. First-principles calculations of charged surfaces and interfaces: a plane-wave non repeated slab approach. *Phys. Rev. B*, 73:115407, 2006.

- [76] M. Otani, I. Hamada, O. Sugino, Y. Morikawa, Y. Okamoto, and T. Ikeshoji. Electrode dynamics from first principles. *J. Phys. Soc. Jpn.*, 77:024802, 2008.
- [77] M. S. Dresselhaus and G. Dresselhaus. Intercalation compounds of graphite. *Adv. Phys.*, 30:139, 1981.
- [78] K. S. Novoselov, A. K. Geim, S. V. Morozov, D. Jiang, M. I. Katsnelson, I. V. Grigorieva, S. V. Dubonos, and A. A. Firsov. Two-dimensional gas of massless dirac fermions in graphene. *Nature*, 438:197, 2005.
- [79] K. I. Bolotin, K. J. Sikes, Z. Jiang, M. Klima, G. Fudenberg, J. Hone, P. Kim, and H. L. Stormer. Ultrahigh electron mobility in suspended graphene. *Solid State Commun.*, 146:351, 2008.
- [80] M. F. Craciun, S. Russo, M. Yamamoto, J. B. Oostinga, A. F. Morpurgo, and S. Tarucha. Trilayer graphene is a semimetal with a gate-tunable band overlap. *Nat. Nanotechnol.*, 4:383, 2009.
- [81] J. O. Sofo, A. S. Chaudhari, and G. D. Barber. Graphane: a two-dimensional hydrocarbon. *Phys. Rev. B*, 75:153401, 2007.
- [82] J. Zhou, M. M. Wu, X. Zhou, and Q. Sun. Tuning electronic and magnetic properties of graphene by surface modification. *Appl. Phys. Lett.*, 95:103108, 2009.
- [83] S. Y. Zhou, G.-H. Gweon, A. V. Fedorov, P. N. First, W. A. de Heer, D.-H. Lee, F. Guinea, A. H. Castro Neto, and A. Lanzara. Substrate-induced bandgap opening in epitaxial graphene. *Nat. Mater.*, 6:770, 2007.
- [84] A. Mattausch and O. Pankratov. Ab Initio study of graphene on SiC. *Phys. Rev. Lett.*, 99:076802, 2007.
- [85] N.-T. Cuong, M. Otani, and S. Okada. Semiconducting electronic property of graphene adsorbed on (0001) surfaces of SiO₂. *Phys. Rev. Lett.*, 106:106801, 2011.
- [86] K. Kamiya, N. Umezawa, and S. Okada. Energetics and electronic structure of graphene adsorbed on HfO₂(111): density functional theory calculations. *Phys. Rev. B*, 83:153413, 2011.
- [87] Y. Takagi and S. Okada. Electronic structure modulation of graphene by metal electrodes. *Jpn. J. Appl. Phys.*, 51:085102, 2012.
- [88] P. Giannozzi, R. Car, and G. Scoles. Oxygen adsorption on graphite and nanotubes. *J. Chem. Phys.*, 118:103, 2003.
- [89] N.-T. Cuong, M. Otani, and S. Okada. Electron-state engineering of bilayer graphene by ionic molecules. *Appl. Phys. Lett.*, 101:233106, 2012.
- [90] E. V. Castro, K. S. Novoselov, S. V. Morozov, N. M. R. Peres, J. M. B. Lopes dos Santos, J. Nilsson, F. Guinea, A. K. Geim, and A. H. Castro Neto. Biased bilayer graphene: semiconductor with a gap tunable by the electric field effect. *Phys. Rev. Lett.*, 99:216802, 2007.

- [91] S. Konabe and S. Okada. Robustness and fragility of a linear dispersion band of bilayer graphene under an electric field. *J. Phys. Soc. Jpn.*, 81:113702, 2012.
- [92] M. Otani, Y. Takagi, M. Koshino, and S. Okada. Phase control of magnetic state of graphite thin films by electric field. *Appl. Phys. Lett.*, 96:242504, 2010.
- [93] Y. Morikawa, K. Iwata, and K. Terakura. Theoretical study of hydrogenation process of formate on clean and Zn deposited Cu(111) surfaces. *Appl. Surf. Sci.*, 169:11, 2000.
- [94] S. Okada, S. Saito, and A. Oshiyama. Energetics and electronic structures of encapsulated C₆₀ in a carbon nanotube. *Phys. Rev. Lett.*, 86:3835, 2001.
- [95] M. Matsubara and S. Okada. Effect of charged metal nanoparticles on carrier injection in graphene by an external electric field. *Appl. Phys. Express*, 10:025101, 2017.
- [96] O. Leenaerts, B. Partoens, and F. M. Peeters. Adsorption of H₂O, NH₃, CO, NO₂ and NO on graphene: a first-principles study. *Phys. Rev. B*, 77:125416, 2008.
- [97] Y. Ma, P. O. Lehtinen, A. S. Foster, and R. M. Nieminen. Magnetic properties of vacancies in graphene and single-walled carbon nanotubes. *New J. Phys.*, 6:68, 2004.
- [98] H. Amara, S. Latil, V. Meunier, Ph. Lambin, and J.-C. Charlier. Molecular doping of graphene. *Phys. Rev. B*, 76:115423, 2007.
- [99] M. M. Ugeda, I. Brihuega, F. Hiebel, P. Mallent, J.-Y. Veullen, J. M. G.-Rodriguez, and F. Yndurain. Electronic and structural characterization of divacancies in irradiated graphene. *Phys. Rev. B*, 85:121402(R), 2012.
- [100] Y. A. Saucier, S. Okada, and M. Maruyama. Strain-induced charge transfer and polarity control of a heterosheet comprising C₆₀ and graphene. *Appl. Phys. Express*, 10:095101, 2017.
- [101] M. Matsubara and S. Okada. Geometric structures of Al nanoparticles adsorbed on graphene under an external electric field. *Jpn. J. Appl. Phys.*, 56:125101, 2017.
- [102] M. Matsubara and S. Okada. Carrier injection in nonbonding π states of N-doped graphene by an external electric field. *Jpn. J. Appl. Phys.*, 56:075101, 2017.
- [103] T. Hussain, T. Kaewmaraya, S. Chakraborty, and R. Ahuja. Defect and substitution-induced silicene sensor to probe toxic gases. *J. Phys. Chem. C*, 120:25256, 2016.
- [104] G. S. Rao, T. Hussain, M. S. Islam, M. Sagynbaeva, D. Gupta, P. Panigrahi, and R. Ahuja. Adsorption mechanism of graphene-like ZnO monolayer towards CO₂ molecules: enhanced CO₂ capture. *Nanotechnology*, 27:015502, 2016.

- [105] D. Wei, Y. Liu, Y. Wang, H. Zhang, L. Huang, and G. Yu. Synthesis of N-doped graphene by chemical vapor deposition and its electrical properties. *Nano Lett.*, 9:1752, 2009.
- [106] X. Wang, X. Li, L. Zhang, Y. Yoon, P. K. Weber, H. Wang, J. Guo, and H. Dai. N-doping of graphene through electrothermal reactions with ammonia. *Science*, 324:768, 2009.
- [107] D. Usachov, O. Vilkov, A. Gruneis, D. Haberer, A. Fedorov, V. K. Adamchuk, A. B. Preobrajenski, P. Dudin, A. Barinov, M. Oehzelt, C. Laubschat, and D. V. Vyalikh. Nitrogen-doped graphene: efficient growth, structure, and electronic properties. *Nano Lett.*, 11:5401, 2011.
- [108] G. Imamura and K. Saiki. Synthesis of nitrogen-doped graphene on Pt(111) by chemical vapor deposition. *J. Phys. Chem. C*, 115:10000, 2011.
- [109] Z. Jin, J. Yao, C. Kittrell, and M. Tour. Large-scale growth and characterizations of nitrogen-doped monolayer graphene sheets. *ACS Nano*, 5:4112, 2011.
- [110] Z. Hou, X. Wang, T. Ikeda, K. Terakura, M. Oshima, M. Kakimoto, and S. Miyata. Interplay between nitrogen dopants and native point defects in graphene. *Phys. Rev. B*, 85:165439, 2012.
- [111] T. Susi, J. Kotakoski, R. Arenal, S. Kurasch, H. Jiang, V. Skakalova, O. Stephan, A. V. Krasheninnikov, E. I. Kauppinen, U. Kaiser, and J. C. Meyer. Atomistic description of electron beam damage in nitrogen-doped graphene and single-walled carbon nanotubes. *ACS Nano*, 6:8837, 2012.
- [112] T. Kondo, T. Suzuki, and J. Nakamura. Nitrogen doping of graphite for enhancement of durability of supported platinum clusters. *J. Phys. Chem. Lett.*, 2:577, 2011.
- [113] T. Kondo, S. Casolo, T. Suzuki, T. Shikano, M. Sakurai, Y. Harada, M. Saito, M. Oshima, M. I. Trioni, G. F. Tantardini, and J. Nakamura. Atomic-scale characterization of nitrogen-doped graphite: effects of dopant nitrogen on the local electronic structure of the surrounding carbon atoms. *Phys. Rev. B*, 86: 035436, 2012.
- [114] Q. Wei, X. Tong, G. Zhang, J. Qiao, Q. Gong, and S. Sun. Nitrogen-doped carbon nanotube and graphene materials for oxygen reduction reactions. *Catalysts*, 5:1574, 2015.
- [115] D. Guo, R. Shibuya, C. Akiba, S. Saji, T. Kondo, and J. Nakamura. Active sites of nitrogen-doped carbon materials for oxygen reduction reaction clarified using model catalysts. *Science*, 351:361, 2016.
- [116] J. Liang, Y. Jiao, M. Jaroniec, and S. Z. Qiao. Sulfur and nitrogen dual-doped mesoporous graphene electrocatalyst for oxygen reduction with synergistically enhanced performance. *Angew. Chem.*, 124:11664, 2012.

-
- [117] M. Levy. Universal variational functionals of electron densities, first-order density matrices, and natural spin-orbitals and solution of the n-representability problem. *Proc. Nat. Acad. Sci. USA*, 76:6062, 1979.
- [118] M. Levy. Electron densities in search of hamiltonians. *Phys. Rev. A*, 26:1200, 1982.
- [119] E. H. Lieb. Density functionals for coulomb systems. *Int. J. Quant. Chem.*, 24: 243, 1983.
- [120] T. L. Gilbert. Hohenberg-Kohn theorem for nonlocal external potentials. *Phys. Rev. B*, 12:2111, 1975.